

Article

CFDs Modeling and Simulation of Wheat Straw Pellet Combustion in a 10 kW Fixed-Bed Downdraft Reactor

Bidhan Nath ^{1,*} , Guangnan Chen ¹ , Les Bowtell ²  and Raid Ahmed Mahmood ³

¹ School of Agriculture and Environmental Science, University of Southern Queensland, Toowoomba, QLD 4350, Australia; guangnan.chen@usq.edu.au

² School of Engineering, University of Southern Queensland, Toowoomba, QLD 4350, Australia; les.bowtell@usq.edu.au

³ Department of Mechanical Engineering, College of Engineering, University of Zakho, Zakho 44001, Iraq; raid.ahmed@uoz.edu.krd

* Correspondence: bidhanbri@gmail.com or u1090250@uemail.usq.edu.au; Tel.: +61-466118046

Abstract: This research paper presents a comprehensive study on the combustion of wheat straw pellets in a 10 kW fixed-bed reactor through a Computational Fluid Dynamics (CFDs) simulation and experimental validation. The developed 2D CFDs model in ANSYS meshing simulates the combustion process in ANSYS Fluent software 2021 R2. The investigation evaluates key parameters such as equivalence ratio, heating value, and temperature distribution within the reactor to enhance gas production efficiency. The simulated results, including combustion temperature and produced gases (CO₂, CO, CH₄), demonstrate a significant agreement with experimental combustion data. The impact of the equivalence ratio on the conversion efficiency and lower heating value (LHV) is systematically explored, revealing that an equivalence ratio of 0.35 is optimal for maximum gas production efficiency. The resulting producer gas composition at this optimum condition includes CO (~27.67%), CH₄ (~3.29%), CO₂ (~11.09%), H₂ (~11.09%), and N₂ (~51%). The findings contribute valuable insights into improving the efficiency of fixed-bed reactors, offering essential information on performance parameters for sustainable and optimized combustion.



Citation: Nath, B.; Chen, G.; Bowtell, L.; Mahmood, R.A. CFDs Modeling and Simulation of Wheat Straw Pellet Combustion in a 10 kW Fixed-Bed Downdraft Reactor. *Processes* **2024**, *12*, 863. <https://doi.org/10.3390/pr12050863>

Academic Editors: Nebojša G. Manić, Bojan Ž. Janković and Dragoslava D. Stojiljković

Received: 7 April 2024
Revised: 19 April 2024
Accepted: 22 April 2024
Published: 25 April 2024



Copyright: © 2024 by the authors. Licensee MDPI, Basel, Switzerland. This article is an open access article distributed under the terms and conditions of the Creative Commons Attribution (CC BY) license (<https://creativecommons.org/licenses/by/4.0/>).

Keywords: biomass; downdraft reactor; Computational Fluid Dynamics; simulation; wheat straw pellets

1. Introduction

Biomass is a reliable alternative energy source used in both developed and developing countries, playing a significant role in global power generation [1]. However, directly using biomass for energy production is often inefficient due to its low energy density, unwanted moisture content, variability in availability, processing requirements, etc. So, a preferred method is to convert biomass into the desired fuel (user-targeted fuel such as solid fuel—pellets, liquid fuel—ethanol, and chemical transport fuel—hydrogen) [2,3]. Various technologies have been developed, like combustion, gasification, and pyrolysis [4]. Combustion, in particular, is a standard method with a high efficiency of up to 50% [5]. Combustion in a downdraft reactor is a promising technology for turning compacted biomass into energy, especially suitable for smaller- to medium-scale power generation [6].

Combustion is less complex than gasification and pyrolysis because it involves a series of chemical reactions in a pyrolysis process [7]. The study of burning waste or biomass in large industrial furnaces is of utmost importance, as demonstrated by the extensive research on grate furnaces [8,9]. However, due to the challenges and costs associated with collecting detailed data from within these furnaces, researchers primarily rely on smaller, fixed-bed units in labs to replicate real-world operations [10]. Experiments and simulation findings support this approach, suggesting a substantial similarity between fixed-bed and grate combustion. The key lies in the minimal horizontal variations within

industrial furnaces compared to the significant vertical changes in the fuel layer. This allows results from fixed-bed experiments, where the fuel bed is stationary. The validity of this approach is further strengthened by the observed similarities in temperature profiles, combustion rates, efficiency, and the gasses released from the fuel bed surface in both setups. As a result, findings from laboratory-scale combustion experiments often need to be more conclusive. Additionally, designing appropriately sized reactors is challenging and requires significant effort and resources. Moreover, the process is time consuming and requires substantial experimental facilities [2]. However, employing a numerical method is an efficient way to gain insights into combustion and understand the fundamental physics involved. Modeling approaches are cost effective, saving time, budget, and resources while facilitating repeatability and justifiable modifications when needed. Various numerical models and simulation tools, including Computational Fluid Dynamics (CFDs), artificial neural networks (ANNs), Aspen Plus (R) or Aspen Hysys equilibrium, and kinetic models have been utilized for combustion in downdraft reactors [6,11–14].

Among various modeling techniques, Computational Fluid Dynamics (CFDs) is considered the most suitable for simulating and predicting the combustion process in fixed-bed reactors due to its ease of operation [14,15]. Many prefer CFDs for scientific research and engineering applications because of its versatility (use of aircraft, submarines, pipes, and such) [16]. Many researchers have reported that several chemical reactions occurred before the gas was produced, becoming non-reactive. In addition, the CFDs model utilizes mass-energy balance and dynamic chemical reactions, enabling it to predict the temperature distribution profile within the combustion zone [17,18]. One significant advantage of CFDs models is their ability to estimate temperature and gas yield throughout the reactor accurately [19]. CFDs models such as pellets are well suited for handling dense particulate matter [20]. Researchers have created two-dimensional (2D) CFDs simulations for both updraft and downdraft reactors in the combustion process [17,21–23]. A review by Patra and Sheth [12] highlighted the challenges of CFDs modeling, specifically in downdraft reactors, indicating that additional effort is needed to address these issues. Therefore, more action is required to solve the problems. Baruah and Baruah [11], in their literature review, emphasized the significance of CFDs simulations for biomass combustion, noting that challenges include handling dense particulate flow and the unique chemistry of combustion.

Researchers have found that Computational Fluid Dynamics (CFDs) modeling can predict kinetic reactions, mass-heat transfer, thermodynamic behavior, and temperature profiles inside reactors with fewer resources and less time [24]. However, the versatility of CFDs simulations is limited by the fundamental physics and characteristics of the combustion process [25]. Its effectiveness in modeling combustion processes, including fluid flow, heat transfer, and chemical reactions, may be limited by factors such as particle dynamics, chemical reaction kinetics, availability of experimental data, and the challenges associated with validation and verification. In a study by Meenaroch and Kerdsuwan [26], a 2D dynamic model for each zone of the downdraft reactor was developed using CFDs. The model considers drying, pyrolysis, oxidation, and reduction zones. It uses CFDs to solve fundamental equations and simulate gas and solid movement within the reactor. The study examines how the air flow rate affects temperature throughout the reactor and the final producer gas composition. Finally, the model is validated with real-world experiments using wood chips as fuel. In another study by Ngamsidhiphongs Ngamsidhiphongs, Pongpesh [27], a 2D CFDs model for the Imbert downdraft reactor was created, investigating the effects of throat-to-reactor diameter relation and the height of the air input nozzle above the throat. Their findings showed variations in tar concentration and maximum temperature based on throat diameter. This study explores primary tar reduction in downdraft biomass reactors using a 2D CFDs model of an Imbert type. The model successfully predicted gas composition and was validated against real-world data. Pandey, Prajapati [2] recently studied a 2D axisymmetric CFDs model of an Imbert downdraft reactor for Ecoshakti biomass pellets. The model effectively predicts key producer gas components (CO, hydrogen, CO₂).

Studies show that an increasing equivalence ratio (ER) in combustion reduces CO, hydrogen, and methane while raising nitrogen and CO₂. Higher ER also correlates with increased reactor temperatures. Also, Wu, Gong [28] used ANSYS Fluent software 2021 R2 in a 2D CFDs model for highly preheated air and steam biomass combustion, employing the Euler–Euler multiphase approach with chemical reactions. They concluded that an external heat source requires a high-temperature combustion system. In another simulation, Chapela, Porteiro [29] modeled fouling in biomass combustion systems. Biomass combustion is important to investigate how to minimize NO_x and nitrous oxide emissions according to a study conducted by Ma, Khan [30]. Álvarez-Bermúdez, Chapela [31] and Zhang, Li [32] developed a CFDs modeling in the fixed-bed combustion of biomass. They found that the combustion varies by several factors, and the efficiency depends on the simulation-targeted products.

According to the literature above, most approaches to fixed-bed reactor technology primarily use wood as the feedstock [33–35]. Some studies have been extended to include crop residue combustion, as seen in the work of Mätzing, Gehrman [36]. However, there has been minimal research on numerical models specifically focused on the combustion process of wheat straw pellets [10,37]. Different types of biomasses have distinct chemical structures and compositions [38]. During the thermochemical process, these compositions degrade at different rates and through various mechanisms, impacting each other [21]. Consequently, developing a combustion model for wheat straw pellets (WSPs) is essential for understanding their burning characteristics.

Moreover, available CFDs models for reactors have limitations, including accurate turbulence models, chemical reaction complexity, and time consumption. In addition, they only investigate a small number of characteristics and features [2,27]. To improve the accuracy and reliability of these CFDs models, assessing the outlet producer gas yield and the impact of the equivalence ratio during CFDs model validation is essential [39]. Since the equivalence ratio influences the gas composition, validation should encompass a range of equivalence ratio values. Therefore, this research aims to bridge the gap by CFDs modeling to elucidate the combustion degradation pathways of wheat straw pellets. This novel investigation will contribute to a deeper understanding of wheat straw burning through combustion and pave the way for its efficient conversion into gas. By acquiring previously unavailable data on wheat straw pellets, this research holds the potential to improve bioenergy production processes significantly.

In this study, we created a Computational Fluid Dynamics (CFDs) model to simulate the combustion of wheat straw pellets (WSPs) in a downdraft fixed-bed reactor. Additionally, we explored the best operational conditions to maximize the gas yield and conversion efficiency during pellet combustion. The research delved into various operating factors, including temperature, pressure, and the distribution of produced gas. The findings from this study can be valuable not only for WSPs but also for other types of biomass and reactors.

2. Materials and Methods

2.1. Fuel Parameters

This research involved developing a Computational Fluid Dynamics (CFDs) model tailored for a 10 kW downdraft reactor, specifically focusing on simulating the combustion processes of wheat straw pellets (WSPs). These pellets were produced using additive mixtures comprising 70% wheat straw (WS), 10% sawdust (SD), 10% bagasse (BC), and 10% biochar (BioC), which was outlined in our previous study [40]. A detailed examination of the WSPs' characteristics was conducted using ultimate and proximate analysis. Furthermore, Thermal Gravimetric Analysis (TGA) was employed using NETZSCH STA 449F3 Jupiter (Erich NETZSCH GmbH & Co. Holding KG, Selb, Germany) for the kinetic analysis of WSPs, yielding $E\alpha$ and $\ln A$ values documented in Table 1 [40].

Table 1. Biomass feedstock physiochemical characteristics.

Pellet Features		Value
Proximate analysis (wt % as received, db)	Moisture	3.50
	Volatile matters	44.51
	Fixed carbon	36.99
	Ash	15.00
	Calorific value, HHV (MJ/kg)	19.06
Ultimate analysis (wt % as received, db)	Carbon	45.97
	Hydrogen	5.22
	Nitrogen	0.72
	Sulphur	0.21
	Oxygen (by difference)	47.88
Density	Apparent density (kg/m ³)	817.71
	Bulk density (kg/m ³)	427.45
In Combustion		
Thermokinetic properties *	Activation of energy, E_{α} (kJ/mol)	418.935
	Pre-exponential factor, A (1/s)	1.76×10^{16}
In Pyrolysis		
	Activation of energy, E_{α} (kJ/mol)	132.868
	Pre-exponential factor, A (1/s)	2.4×10^4

Note: * devolatilization phase and heating rate 20 °C/min.

2.2. Reactor—The Central Part of the Reactor

Reactors are tools used to convert solid biomass material into gaseous fuel [41]. Two widely employed configurations for fixed-bed reactors are the downdraft (co-current flow) and updraft (cross-current flow) approaches, distinguished by the relative movement of the feedstock and combustion agent [42]. In the downdraft reactor, biomass enters from the top, air flows from the side, and a multi-stage combustion process (primary, intermediate, and dilution zones) efficiently converts the biomass into gas [43]. Drying and pyrolysis, the thermal decomposition of biomass, occur simultaneously within the reactor. Finally, the temperature is reduced for the reduction stage. Interestingly, the downdraft reactor's geometry proves versatile, applying it to combustion and gasification processes [44].

The reactor, a central component of the reactor, is built-in and has an overall height and diameter of 660 mm and 375 mm, respectively. The feedstock is introduced into the reactor from the top for the combustion process, while air is injected through nozzles from both sides. The bottom of the reactor releases outlet gases and char-rich ash. Figure 1 presents a diagram of the reactor illustrating zones and immediate production formation.

2.3. Modeling Theory—Thermochemical Conversion of Solid Fuel

In combustion modeling, the key focus is understanding particle movement in gas and solid phases [43]. Solid particles and gases move in the same direction in a downdraft reactor. The combined volume of solids and gases equals the total volume. However, the total particle area changes with the height of the bed. Additionally, the composition of gases and solids shifts throughout the bed. Consequently, the model's reactor bed experiences the movement of both solid and gas phases. Figure 2 illustrates the particles involved in the plug flow regime.

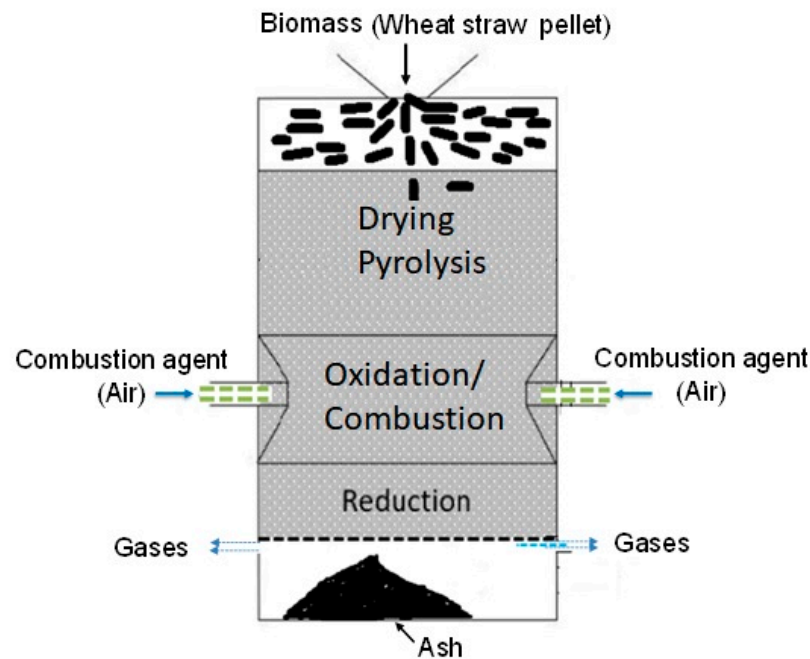


Figure 1. Reactor zone and transitional product formation.

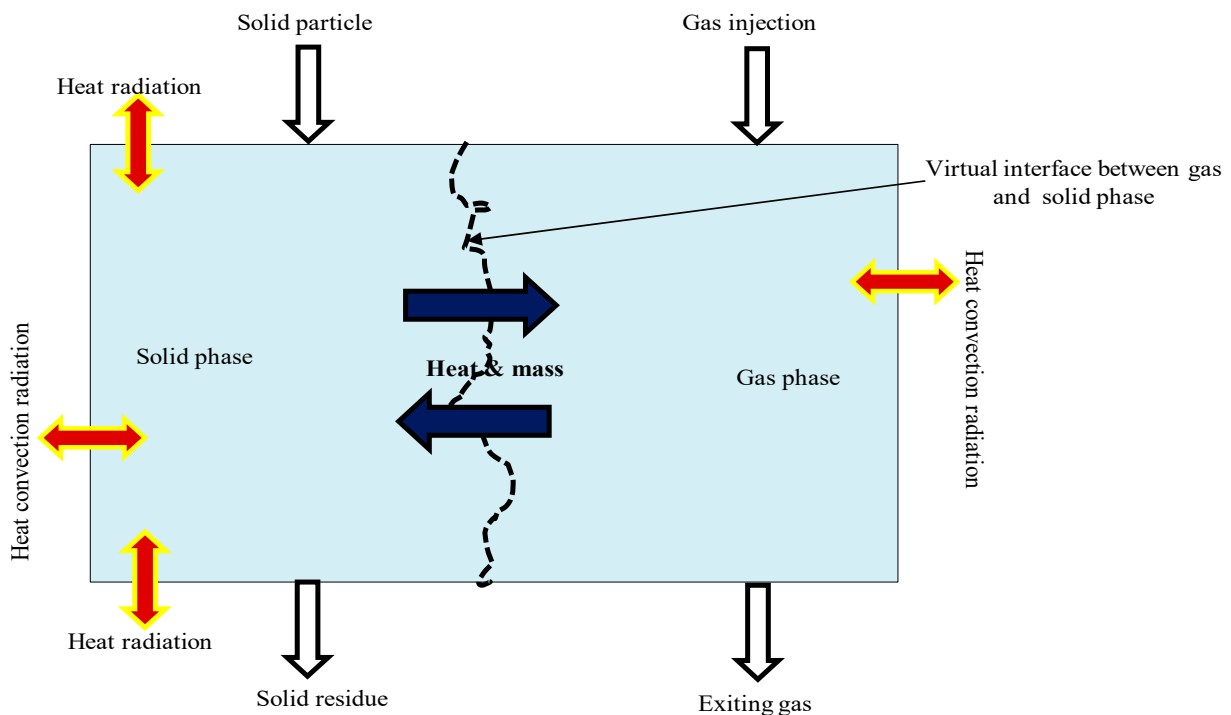


Figure 2. Modeling scheme of solid fuel in a fixed-bed downdraft reactor.

2.4. CFDs Model Development

The downdraft reactor model was created using a 2D planar configuration with ANSYS Fluent 2021 R2. Figure 3 illustrates the Computational Fluid Dynamics (CFDs) simulation process.

Following the five steps outlined by Nørregaard, Bach [45] is essential to develop the model. The initial step is pre-processing, involving the definition of geometry. Meshing requirements are then established to ensure the geometry's independence is tested. Simultaneously, Probability Density Functions (PDFs) are constructed to represent the mixture

of products in gases. Following this, the primary boundary conditions are defined, with wheat straw pellets (WSPs) as the fuel input and air as the combustion agent. Lastly, the analysis and interpretation phase outlines the post-processing technique.

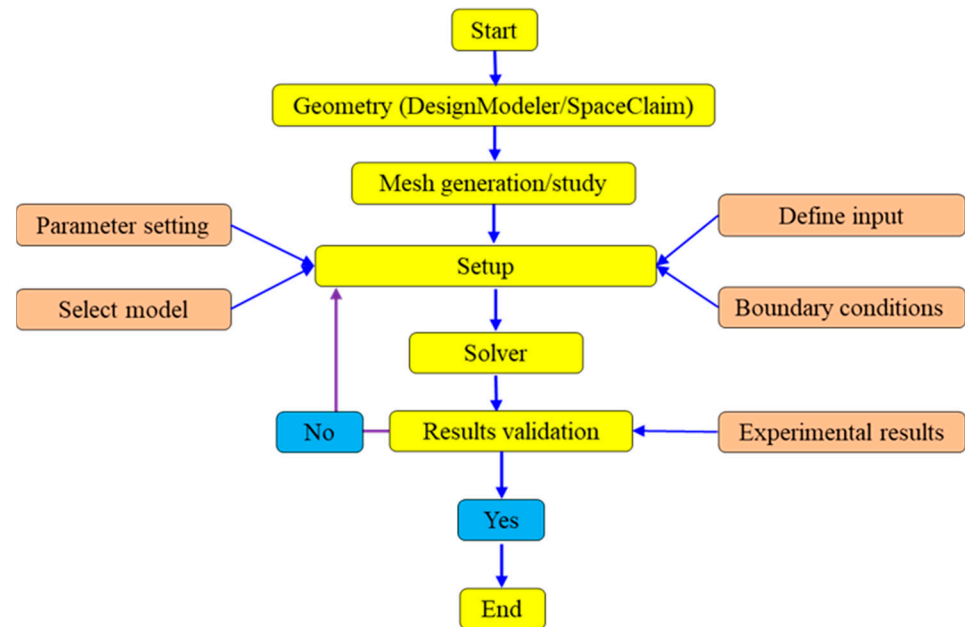


Figure 3. Flowchart for numerical simulation of combustion using Computational Fluid Dynamics.

2.4.1. Geometry Construction

Geometry is a crucial and fundamental aspect of the simulation process [46]. Initially, geometry was constructed to replicate an in-built downdraft reactor reactor. For this purpose, the Design Modeler Program (DMP) within the ANSYS Workbench 2021.1R2 was employed to establish the geometry domain. The 2D planar representation of the geometry is illustrated in Figure 4a.

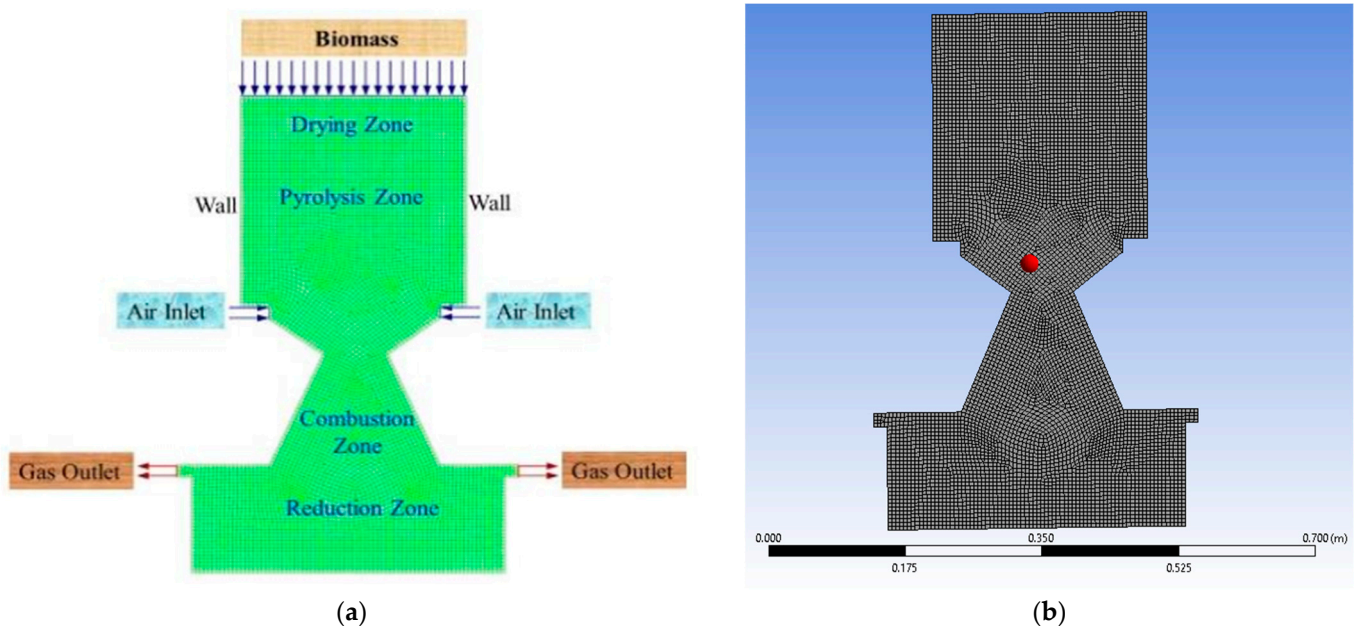


Figure 4. Visualization of geometry and mesh details. (a) Reactor geometry (2D Planner). (b) Reactor mesh details of a 2D model: black represents the insulation (dimensions are in m).

2.4.2. Mesh Generation

Creating high-quality meshes is crucial for achieving accurate and rapidly converging Computational Fluid Dynamics (CFDs) simulations [47]. The ANSYS Meshing package generated and optimized the mesh, employing a global tool to obtain an unstructured grid. Several tests were conducted on local sizing parameters to ensure favorable mesh quality. Figure 4b displays the generated model mesh. In general, it is recommended to maintain a minimum orthogonal quality of >0.10 and a maximum skewness of <0.95 for good mesh quality. However, these values may vary based on the physics and location of all cells.

Refinement is a beneficial technique for capturing steep flow gradients, especially in highly turbulent regions [48]. Consequently, the mesh in the combustion, reduction, and air nozzle outlet areas was refined.

2.4.3. Model Setting

Model Selection

Various physicochemical phenomena, primarily decomposition related, occur throughout the combustion process. These decomposition factors encompass the release of water, volatile flammable gases, heat conduction, fissuring, shrinkage, and the fragmentation of solid particles [49]. The interaction between the input biomass and air inside the reactor involves different activities, as outlined in various models (Table 2). Additionally, the interaction between heat and particle mass within the reactors results in different chemical kinetic reactions as specified by the governing equations.

Table 2. Representation of the model, including air, biomass, and reactor, during the combustion process.

Components	Computational Model
Biomass	- Discrete phase model (DPM)
	- $k - \epsilon$ turbulence
	- P-1 for radiation model
Air	- Resistance flow
	- Turbulence flow model
	- Porous media model
Combustion	- Lagrangian discrete phase model
	- Turbulence–chemistry interaction model
	- Energy and species transport equations

Model Simplifications

Combustion encompasses numerous intricate processes that involve both homogeneous and heterogeneous reactions. Several simplifications were necessary to develop a suitable model for a downdraft reactor. The extent of simplification relies on the specific goals of the model. Several general assumptions were made to simplify the model, as guided by the work of Gupta, Jain [50].

The flow within the system is characterized by symmetry in a two-dimensional space. It maintains a steady state, and the governing equations for numerical calculations involve nonlinear partial differential equations. The reactor wall's surface and the materials constituting the separator/insulation adhere to the no-slip condition. Chemical reactions within the system occur faster than the time scale of turbulence eddies. A discrete phase model compares small particle sizes to the reactor volume. All chemical reactions are assumed to occur within the reactor's inner shell. The particles in the system exhibit a uniform distribution and spherical shapes, with a size considerably smaller, measuring 0.1 mm. The oxidizer utilized in the process is air.

2.5. Solution of Model-Based Equations

The ANSYS Fluent CFDs software 2021 R2 package employs in-house C coding through a User-Defined Function (UDF) [51]. This allows for the straightforward trans-

formation of partial differential equations into a discrete form using CFDs, facilitating the solution of conservation equations. CFDs operates on a simultaneous calculation set for governing equations and species conservation. On the other hand, the Finite Element Method (FEM) can be utilized for discretization, with ANSYS Fluent 2021 R2 customizing the Finite Volume Method [52]. The solution process also involves implementing a pressure–velocity coupling technique to address the governing equation.

2.5.1. Governing Equation: Pressure–Velocity Coupling Method

The CFDs model includes governing equations for species transfer within the fluid flow. The species are categorized into two phases: gas (primary flow) and solid (secondary flow). A Euler–Euler multiphase technique is employed to solve the phases, incorporating exchange terms [53]. The equations are numerically solved under steady-state and turbulent flow conditions, with finite-rate reaction kinetics, as outlined in [2].

$$\frac{\partial(\rho\mu_i)}{\partial t} + \frac{\partial(\mu_i\mu_j)}{\partial x_i} = -\frac{\partial\rho}{\partial x_j} + \frac{\partial\tau_{ij}}{\partial x_i} + p\sum_{k=1}^N Y_k f_{kj} \quad (1)$$

$$\tau_{ij} = -\frac{2}{3}\mu\frac{\partial u_k}{\partial x_k}\delta_{ij} + \mu\left(\frac{\partial\mu_i}{\partial x_j} + \frac{\partial\mu_j}{\partial x_i}\right) \quad (2)$$

$$\frac{\partial\rho}{\partial t} + \frac{\partial(\rho\mu_i)}{\partial x_i} \quad (3)$$

$$\frac{\partial(\rho Y_k)}{\partial t} + \frac{\partial}{\partial x_i}[\rho Y_k(\mu_i + V_{ki})] \quad (4)$$

$$\frac{\partial(\rho e_t)}{\partial t} + \frac{\partial}{\partial x_i}(\rho\mu_i e_t) = -\frac{\partial q_i}{\partial x_i} + \frac{\partial}{\partial x_j}[(\tau_{ij} - \rho\delta_{ij})u_i] + \dot{Q} + \rho\sum_{k=1}^N Y_k f_{ki}(\mu_i + V_{ki}) \quad (5)$$

$$q_i = -k\frac{\partial T}{\partial x_i} + \rho\sum_{k=1}^N (h_k Y_k V_{ki}) \quad (6)$$

where ρ = the density of the fluid mixture;

t = time;

p = pressure;

$\mu_i\mu_j$ = the velocity components;

τ_{ij} = the viscus stress tensor;

Y_k = the mass fraction of species k in the fluid mixtures;

f_{kj} = the volume force acting on species k in the j direction;

$x_i x_j$ = the coordinates axes;

V_{ki} = the i -component of the diffusion velocity of species k ;

ω_k = the reaction rate of species k ;

q_i = energy flux in the mixture;

e_t = total energy from chemical, potential and kinetic energies;

\dot{Q} = energy flux from the outer heating source.

The standard $k - \epsilon$ turbulence model was applied to the gas phase. The kinetic turbulence energy (k) and its dissipation rate (ϵ) were obtained from the following equations [54]:

$$\frac{\partial}{\partial x_i}(\rho k\mu_i) = \frac{\partial}{\partial x_j}\left[\left(\mu + \frac{\mu_t}{\sigma_k}\right)\frac{\partial k}{\partial x_j}\right] + G_k + G_b - \rho\epsilon - Y_m + S_k \quad (7)$$

$$\frac{\partial}{\partial x_i}(\rho\epsilon\mu_i) = \frac{\partial}{\partial x_j}\left[\left(\mu + \frac{\mu_t}{\sigma_\epsilon}\right)\frac{\partial \epsilon}{\partial x_j}\right] + C_{1\epsilon}\frac{\epsilon}{k}(G_k + C_{3\epsilon}G_b) - C_{2\epsilon}\rho\frac{\epsilon^2}{k} + S_\epsilon \quad (8)$$

where G_b = turbulence kinetic energy due to buoyancy;

Y_m = fluctuation dilation in compressible turbulence;
 S_k = user-defined source terms for k ;
 S_ϵ = user-defined source term for ϵ ;
 σ_k = turbulent Prandtl numbers for k ;
 σ_ϵ = turbulent Prandtl numbers for ϵ .

G_k denotes the kinetic turbulence energy production, which is linked to the average velocity gradient and μ_t = Turbulence viscosity (or eddy), which is obtained from the value of k and ϵ :

$$\mu_t = \rho C_\mu \frac{k^2}{\epsilon} \quad (9)$$

The constants of the experimental model are equal to $C_{1\epsilon} = 1.44$, $C_{2\epsilon} = 1.92$, $C_{3\epsilon} = 0.09$, $\sigma_k = 1.0$, $\sigma_\epsilon = 1.3$ [55].

2.5.2. Energy and Species Transport Equation

The species model serves as a tool to explore the chemical reactions occurring within the reactor, providing insights into the composition of different species like CO, CO₂, N₂, H₂, and CH₄ [56]. Consequently, the species transport equations and enthalpy formations are employed to calculate the chemical reactions, following the approach outlined by Magnussen and Hjertager [57].

$$\text{Enthalpy, } H = h + \Delta H \quad (10)$$

$$h = h_{ref} + \int_{T_{ref}}^T c_p dT \quad (11)$$

$$\text{Species transport equation, } \frac{\partial}{\partial t}(\rho Y_i) + \nabla \cdot (\rho \vec{\mu} Y_i) = -\nabla \cdot \vec{J}_i + R_i + S_i \quad (12)$$

$$\text{Energy balance equation, } \rho C_p \frac{\partial T}{\partial t} = k \nabla^2 T + qv \quad (13)$$

where: h = sensible enthalpy;

ΔH = latent heat enthalpy;

h_{ref} = reference enthalpy;

T_{ref} = reference temperature;

C_p = specific heat at constant pressure;

R_i = net rate of production of species, i ;

S_i = source term for the i th (x, y, z) momentum equation;

Y_i = species i 's average mass fraction;

R_i = net rate of production of species " i " by chemical reaction.

2.5.3. Particle Combustion Model

Both the Euler–Lagrange and Euler–Euler approaches can address particle interaction [58]. The Euler–Euler approach, identified as multiphase, contrasts with the Euler–Lagrange system, also known as the Discrete phase [59]. This study specifically utilized the Discrete phase. Experimental data on WSPs, denoted as $E\alpha$ and A , were incorporated into the model to anticipate their decomposition rate. The investigation involved considerations of the particle force balance equation, heat balance equation, and the devolatilization law balance equation, as delineated by Pandey, Prajapati [2].

- Force balance equation

$$\frac{\partial}{\partial t}(\vec{\mu}_\rho) = F_D(\vec{\mu} - \vec{\mu}_\rho) + \frac{\vec{g}(\rho_p - \rho)}{\rho_p} \quad (14)$$

$$\text{Drag force } F_D = \frac{18\mu C_D Re}{24\rho_p d_p^2} \quad (15)$$

where $F_D(\vec{\mu} - \vec{\mu}_p)$ is drag force per unit particle mass.

- Particle heat balance equation

$$m_p C_p \frac{\partial T_p}{\partial t} = h A_p (T_\infty - T_p) + \varepsilon_p A_p \sigma (T_R^4 - T_p^4) \quad (16)$$

- Heat transfer during the devolatilization process

Upon reaching the vaporization temperature (T_{vap}), the devolatilization law is applied to the mass of the combusting particle (m_p) [54]. It is written as

$$m_p C_p \frac{\partial T_p}{\partial t} = h A_p (T - T_p) + \frac{\partial m_p}{\partial t} h_{fg} + \varepsilon_p A_p \sigma (T_R^4 - T_p^4) \quad (17)$$

$$-\frac{\partial m_p}{\partial t} = A e^{-\left(\frac{E}{RT}\right)} \left[m_p - (1 - f_v^0) m_p^0 \right] \quad (18)$$

where: f_v = volatile fraction and m_p^0 = initial mass.

- Heat transfer during the char conversion process

Convection, radiation, and heat loss contribute to heat transfer to the particle during devolatilization [60]. It is written as

$$m_p C_p \frac{\partial T_p}{\partial t} = h A_p (T_\infty - T_p) + f_h \frac{\partial m_p}{\partial t} h_{fg} + \varepsilon_p A_p \sigma (T_R^4 - T_p^4) \quad (19)$$

where C_p , h_{fg} , A , and σ are the specific heat, latent heat of evaporation, particle surface area, and Stefan constant, respectively.

2.5.4. Radiation Model

The P-1 model is generally more effective in combustion applications characterized by large optical thickness, intricate geometries with curved coordinates, and radiation heat transfer considerations [61]. The calculation of the radiation flux (q_r) is based on the P-1 model, as expressed by the equation outlined by Wang and Yan [18]:

$$q_r = -\frac{1}{3(\alpha + \sigma_s) - C\sigma_s} \nabla G \quad (20)$$

$$\nabla q_r = \alpha G - 4\alpha\sigma T^4 \quad (21)$$

where: α = absorption coefficient;

σ_s = Stefan–Boltzmann constant;

G = incident radiation;

C = linear-anisotropic phase function coefficient [54].

2.5.5. Chemical Reaction Model

Devolatilization stands out as the key decomposition process in biomass combustion [53]. This process encompasses homogeneous and heterogeneous approaches, incorporating a chemical reaction model outlined by Gupta, Jain [50]. The reaction model, applied to downdraft combustion, involves four stages: drying, pyrolysis, combustion, and reduction [54]. Modeling the feedstock pyrolysis rate employs a straightforward one-step reaction model, as proposed by Di Blasi [62]. Meanwhile, combustion in the three primary oxidation zones (R_g2 , R_g3 , and R_s8 , as detailed in Table 3) is considered according to the work of Janajreh and Al Shrah [63]. The products from oxidation and pyrolysis zones are transformed into gases within the reduction zone through heterogeneous and homogeneous processes (R_g4 , R_s5 , R_s6 , R_s7 , R_s8 , and R_s9 , as shown in Table 3).

Table 3. Solid particle surface reactions.

Gas Phase Reaction		Solid Particle Surface Reactions	
Reaction	Reaction Order	Reaction	Reaction Order
Volatile decomposition	R_g1	Char decomposition	R_s5
CO combustion : $2CO + O_2 \rightarrow 2CO_2$	R_g2	$C_{(s)} + O_2 \rightarrow CO_2$	R_s6
H ₂ combustion : $2H_2 + O_2 \rightarrow 2H_2O$	R_g3	$C_{(s)} + O_2 \rightarrow 2CO$	R_s7
Water–gas shift : $CO + H_2O \rightarrow$ $CO_2 + H_2$	R_g4	$C_{(s)} + 2H_2 \rightarrow CH_4$	R_s8
		$C_{(s)} + H_2O \rightarrow CO + H_2$	R_s9

2.6. Boundary and Operating Conditions Setup

In this study, the delineation of primary and secondary steps was contingent upon the two-phase flow pattern, with the solid phase identified as primary and the gas phase as secondary. Ensuring reliable simulations necessitated careful consideration of operating and boundary conditions, beginning with selecting the reaction phase. The boundary and operating conditions for the combustion of WSPs in downdraft reactors were derived from a combination of experimental operations and data from the literature [42]. A summary of these operating conditions is provided in Table 4.

Table 4. Boundary and operating conditions of the biomass CFDs model to ensure accurate simulations.

	Parameter	References
Combustion agent (air)	Air flow rate: 54 kg/h (37.87 Nm ³ /h)	-
	Air velocity: 3.2~7.2 m/s (average 5.2)	[50]
	Air fuel ratio: 6:1 v/m	[63]
	Air inlet temperature: 300 K	[50]
Pressure	Combustion pressure: 1 atm = 101,325 pascal	[6]
	Outlet gauge pressure: 0	[42]
	Pressure outlet: 249 pascals (min) and 747 pascals (max)	-
Biomass	Input: biomass (WSPs) inject (gravity feed)	-
	Gravitational acceleration: -9.8 m/s^2	-
	Biomass inlet temperature: 300° K	[2]
	Biomass flow rate: 9 kg/h	[50]
	Biomass moisture content: 3.5%	-
Temperature	Temperature—atmospheric condition: 300 K	[42]
	Operating temperature: 300~2500 K	-
Reactor wall	Motion: stationary	
	Wall shear condition: no slip	[42]
	Wall roughness: standard	
	Inlet species mass fraction of O ₂ : 0.23	[42]
	Inlet velocity magnitude: 0.056 m/s	-
	Wall (interior and exterior walls): stainless steel	-
	Wall thickness: 3 mm	-
Others	Equivalence ratio: 0.2~0.6	[33]
	Turbulence intensity: 5%	[42]
	Particle-specific heat: 2.5 kJ/kgK	[42]
	Particle size in the discrete phase: 0.1 mm	[2]
	Uniform porosity: 0.5	[64]
	For simulation time setup: 10 s	[42]
	Model run: 0 to 7200 s	

2.7. Input Data for Simulations

The simulation input data were derived from experimental results and the prior literature, as presented in Tables 4 and 5. Initially, the combustion characteristics of pellet fuels were defined through ultimate and proximate analyses, which had been conducted previously [40]. Additionally, the pellet's apparent density was specified as the particle

density and incorporated into the material input. Moreover, a shrinkage coefficient of 0.6, derived from experimental results on pellets (empty fruit bunch), was utilized in the downdraft reactor [65]. Notably, the ANSYS Fluent 2021 R2 template utilized the swelling coefficient as the counterpart to the shrinkage coefficient.

Table 5. Summary of the model used for the combustion of wheat straw pellets.

Parameters	Conditions/Assumptions
1. General	✓ Double precision: two-phase flow (gas and solid) simulation
	✓ Solver type: pressure based
	✓ Velocity formulation: absolute
	✓ Steady-state
	✓ Axisymmetric/planner
2. Radiation	✓ Gravitational effect on biomass feeding
	P1: radiation reflection at the surface is isotropic
3. Turbulence	SST $k\omega$ -intermittency: include the effect of share stress transport, kinetic, its dissipation rate, and the change in velocity
4. Reactions	Nonpremix combustion-non-adiabatic
5. Particle interaction	Euler–Lagrange (discrete phase)
	Particle devolatilization model: single kinetic rate Particle combustion: kinetic/diffusion-limited rate

In the simulation of fixed-bed combustion, air injection occurred through a side nozzle, characterized by its velocity (m/s). Conversely, the feedstock fuel mass was introduced from the top, and the feedstock material, in the form of cylindrical pellets, deviated from a spherical shape. As a result, the equivalent diameter was computed based on the pellet volume, following the approach outlined by Erlich and Fransson [65]:

$$D_E = 2 * \sqrt[3]{\frac{3}{4\pi} V_p} \quad (22)$$

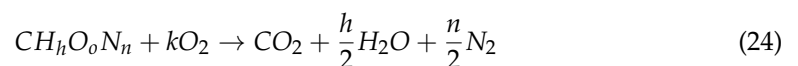
where: D_E = particle diameter (m)

V_p = average volume of a particle (m^3)

The equivalence ratio (ER) is the proportion of the combustion model (AF_{model}) air-to-fuel ratio to the stoichiometric air–fuel ratio for complete combustion ($AF_{stoichiometric}$) [66].

$$ER = \frac{\text{Actual air to biomass ratio}}{\text{Stoichiometric air to biomass ratio}} = \frac{AF_{model}}{AF_{stoichiometric}} \quad (23)$$

The $AF_{stoichiometric}$ can be calculated based on the empirical formula, which is based on the ultimate fuel analysis data.



$$k = \frac{h}{4} + 1 - \frac{O}{2} \quad (25)$$

where k = number of moles of oxygen for complete combustion;

h = mole fraction of hydrogen in fuel;

O = mole fraction of oxygen in a fuel.

In combustion, the oxidizing agent was air with a ratio of 4.76 of air to oxygen [67]. Then, the stoichiometric air-to-fuel ratio ($AF_{stoichiometric}$) is determined as

$$\text{Stoichiometric air-to-fuel ratio} \left(\frac{A}{AF_{stoichiometric}} \right) = \frac{4.76 * k * mw_{ox}}{mw_{fuel}} \quad (26)$$

where k = the number of moles of oxygen for complete combustion;
 mw_{ox} = molecular weight of oxygen in the air (g/mol);
 mw_{fuel} = molecular weight of fuel (g/mol).

2.8. Numerical Calculation

Two approaches exist within the ANSYS Fluent 2021 R2 Solver program: pressure based and density based. This study employed the pressure-based technique, the default solver in the non-premix combustion model, as indicated in Table 6 [68].

Table 6. Particulars of the biomass CFDs model solver.

Variable	Discretization Scheme	Information
Pressure-staggering option	PRESTO!	Pressure-based Navier–Stokes solution algorithm (the default)
Pressure–velocity coupling	SIMPLE	Governing equation
Gradient option	Least Squares Cell based	-
Pressure	Second-order Upwind	Spatial discretization
Momentum	Second-order Upwind	Spatial discretization
Turbulent Kinetic Energy	Second-order Upwind	Spatial discretization
Turbulent Dissipation Rate	Second-order Upwind	Spatial discretization
Energy	Second-order Upwind	Spatial discretization
Mean mixture fraction	First-order Upwind	Spatial discretization
Mixture fraction variance	Second-order Upwind	Spatial discretization
Soot	Second-order Upwind	Spatial discretization
Others	First-order Upwind	-
Discrete ordinates	Second-order Upwind	Spatial discretization
Formulation	Implicit	-
Velocity formulation	Absolute	default setting
Porous formulation	Superficial velocity	-
Initializations	Hybrid	-

2.9. Gas Production and Gas Efficiency

In theory, the concentration of carbon-containing gases such as CO, CH₄, and CO₂ tends to increase with higher carbon content in the feedstock during air combustion. The heating value and produced gas efficiency were calculated as follows:

$$LHV_{gas} = (Y_{CO} \times 13.1) + (Y_{CH_4} \times 37.1) + (Y_{H_2} \times 11.2) \quad (27)$$

$$E_{ff_{gas}} = \frac{HV_{gas} \times F_{gas}}{HV_{fuel}} \quad (28)$$

where $E_{ff_{gas}}$ = production gas conversion efficiency (%);

HV_{fuel} = heating value of fuel (MJ/m³);

LHV_{gas} = lower heating value of gas (MJ/m³);

F_{gas} = production gas–fuel feed ratio (m³/kg);

Y = mole fraction of the gas;

3. Results and Discussion

3.1. Grid Sensitivity Analysis

A grid dependency or sensitivity test was conducted to determine the optimal number of mesh elements, as outlined by Pandey, Prajapati [2]. This test assesses the impact of mesh density on simulation results and aids in estimating computational resource consumption [69]. While ANSYS Fluent 2021 R2 allows the generation of tetrahedral and hexahedral meshes, this study opted for a hexahedral mesh because of its superior quality and faster computation times.

A total of 5 distinct computational grid sets were generated, comprising 5000, 10,000, 25,000, 50,000, and 100,000 cells for the dependency test. For grid generation, the test considered a single boundary condition. The initial conditions assumed the reactor interior as a porous medium without chemical reaction. Air served as the combustion agent, with a mass flow of 54 kg/h and a pressure outlet to account for the boundary condition (Table 4). The grid dependency test focused on velocity measurements at various reactor planes. Figure 5 illustrates the velocity distribution along the reactor at a distance of 660 mm from the top for the 5 mesh element variations. As depicted in Figure 6, all mesh cells exhibited a consistent trend, with the velocity increasing along the shifted position.

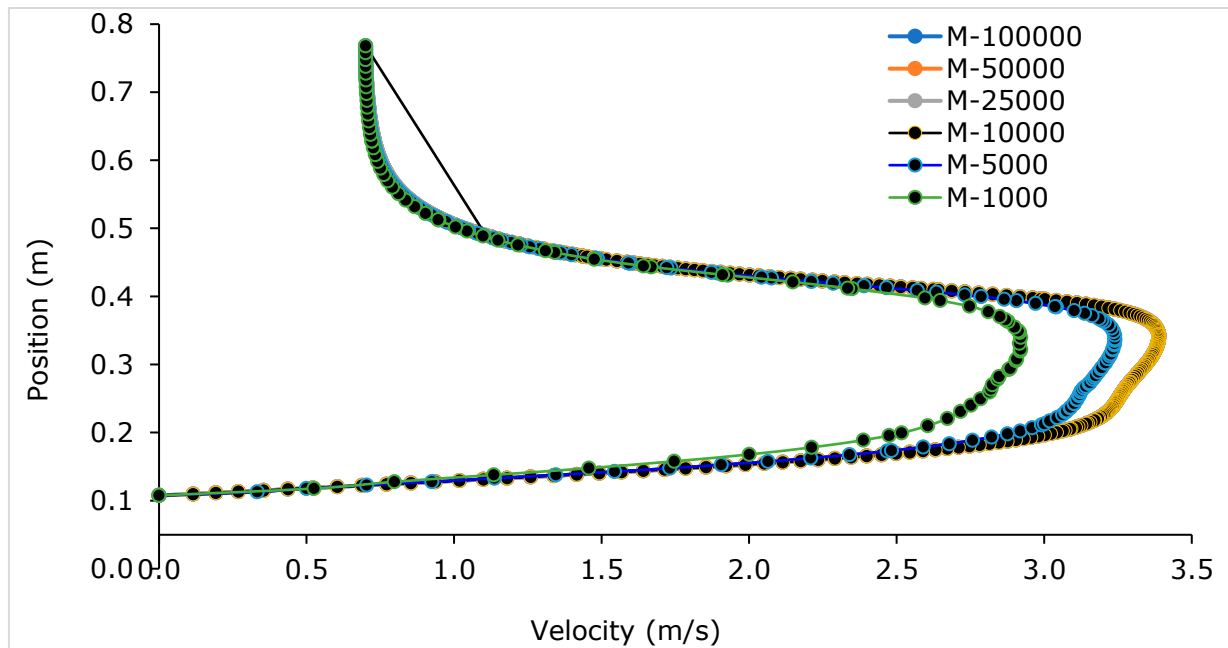


Figure 5. Relation between velocity and vertical position of reactor regarding mesh elements.

Figure 6 illustrates a marginal velocity difference between 25,000 and 50,000 mesh cells, averaging less than 2%. It is evident that there was no substantial alteration in velocity as the mesh number exceeded 50,000. Consequently, the optimal number of mesh elements was determined to be 50,000, representing the combustion phenomena with the most effective combination, as noted by Murugan and Sekhar [70]. Table 7 presents the details of simulated model statistics.

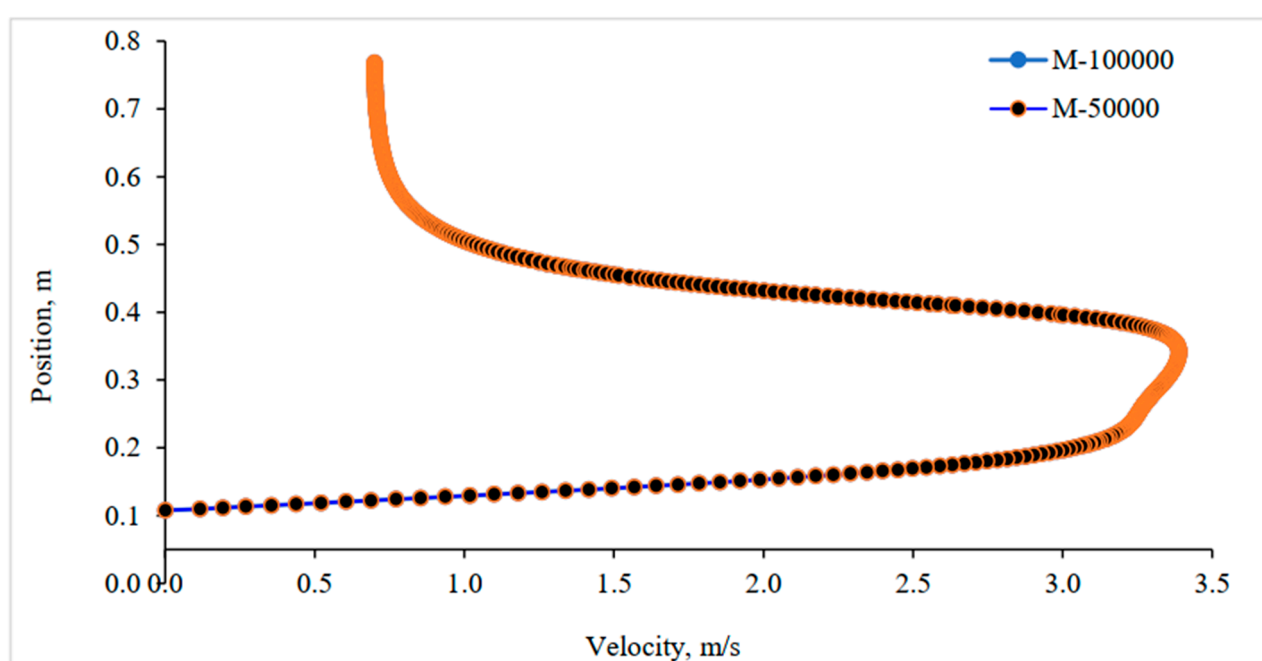


Figure 6. Velocity comparison between the grid cells.

Table 7. Simulated mesh cells, and mesh statistics of developed model.

Particulars	Value
Mesh element size (average)	1 mm
No. of nodes	172,677
No. of elements	171,558 with a rectangular shape
Minimum orthogonal quality	0.38916
Maximum aspect ratio	5.27929

3.2. Model Validation and Comparison

Validation of the developed model is imperative for assessing its accuracy. Numerous researchers have validated the model using experimental data and published results. In this study, validation was conducted by comparing the model predictions with relevant experimental data.

Experimental Details on Combustion

To validate the model in this study, a combustion experiment involving WSPs was conducted using a GEK 10 kW downdraft reactor located at UniSQ, Australia (<http://www.allpowerlabs.com>). A corresponding Computational Fluid Dynamics (CFDs) model was developed for the same reactor and designed to accommodate various fuels with users inputting the fuel (feedstock) property data.

The experimental results were utilized for model validation, focusing on the temperature within the combustion zone and the gas composition. Two thermocouples were strategically placed to record temperatures within the reactor bed. The thermocouple T_{red} was positioned in the higher portion of the reactor concentric space to represent the temperature of the combustion zone. At the same time, T_{bred} was placed in the lower part to represent the temperature of the reduction zone. An online gas infrared analyzer was also installed on the gas output pipe to monitor CO, CO₂, and total hydrocarbon contents (HC).

Figure 7 illustrates the gas composition and temperature data. After 70 min of combustion running time, the experiment reached a stable state with the optimum temperature,

revealing a combustion zone (T_{red}) temperature of around 1200~1250 K, and the reduction zone (T_{bred}) temperature was about 1000~1083 K. The obtained gas composition at steady-state operation comprised approximately 9% CO₂ and 23% CO (Figure 7).

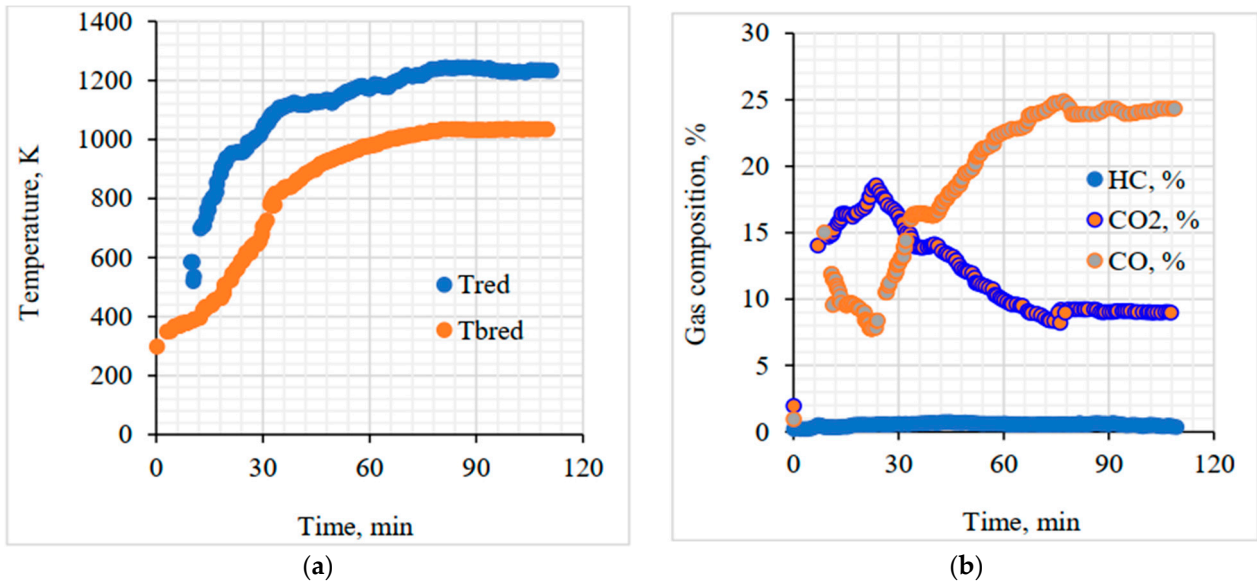


Figure 7. Combustion experimental results. (a) Relationship between combustion retention time. (b) Relationship between combustion retention time and produced gas composition.

Figure 8 illustrates the simulation output within the vertical iso-surface of the reactor at $Y = 1.5$ mm, positioned near the central axis of symmetry. The model simulation incorporated an air/fuel ratio of 6 (v/m) and an equivalence ratio (ER) of 0.25. The baseline temperature for the simulation was found at 1413.22 K.

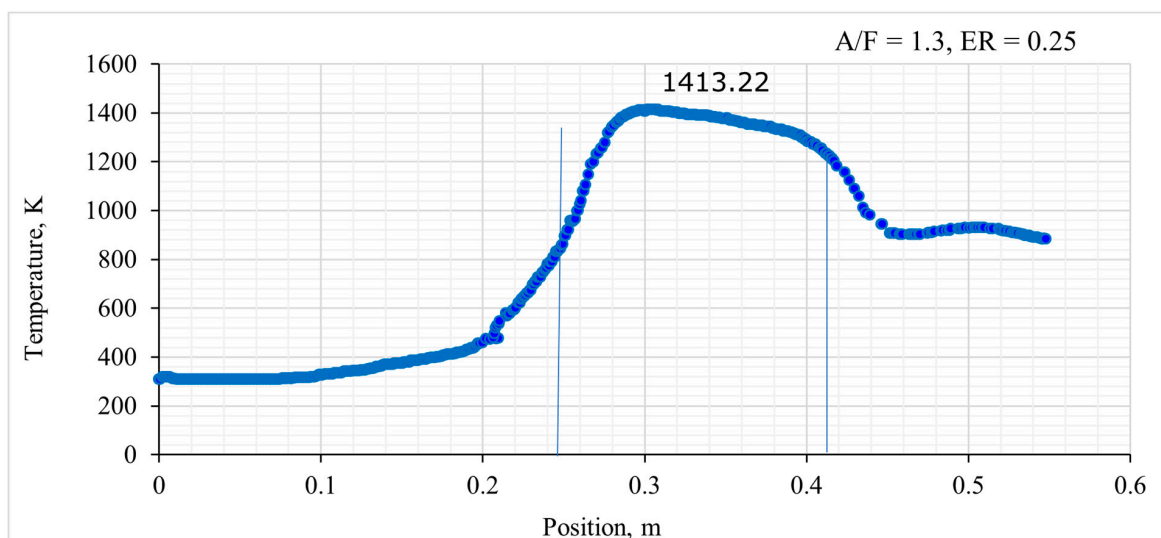


Figure 8. Iso-surface representing the temperature in the CFDs model results for combustion.

Table 8 summarizes experimental data and modeling results. The simulated temperature and volume of gas species closely resembled the experimental measurements. While the values for CO₂ and CH₄ were slightly higher than the experimental data, the concentration of CO was relatively underestimated. However, the prediction of high hydrogen concentration remained unverified. Despite these minor discrepancies, the simulations

aligned satisfactorily with previous experimental data regarding temperature patterns and gas composition. Therefore, the overall accuracy of the model was deemed acceptable.

Table 8. Result comparison: CFDs combustion model.

	Particulars	Results	
		Model	Experiments
Temperature (K)	Combustion (Upper concentric at $x = 0.25$ to 0.3 m)	900~1413	1250
	Reduction (Bottom reduction at $x = 0.425$ m)	1100	1080
Gas species (% v/v)	CO ₂	9.99	9.4
	CO	21.60	23.3
	CH ₄	0.13	0.051
	H ₂	16.81	N/A

3.3. Prediction Profile and Gas Distribution

In combustion, biomass initially enters the pyrolysis zone before moving into the combustion zone, as illustrated in Figure 9. The combustion zone extends to the neck of the concentric area from beneath the air inlet. Eventually, the pressure outlet releases the gas, while the remaining particles (char and ash) descend the grate. These residual char and ash particles continue to participate in oxidation and reduction processes, as described by Pandey, Prajapati [25].

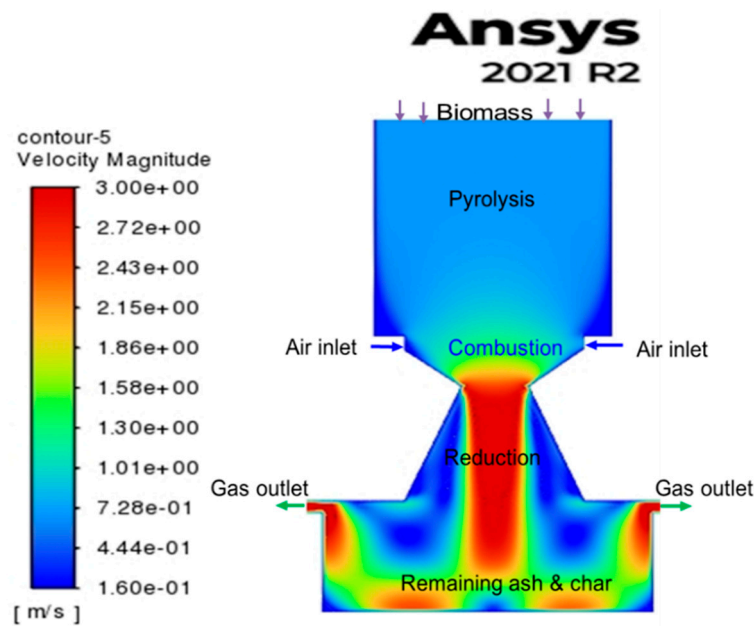


Figure 9. Model interpretation of velocity contour.

The initial step in combustion involves the input of biomass, initiating the production of gases that are subsequently distributed throughout the reactor. As biomass enters the reactor, it breaks into volatile and char components. According to the volatile disintegration scheme, the volatile fraction decomposes into CO, H₂, CH₄, CO₂, and H₂O. These volatiles (CO, H₂, and CH₄) meet oxygen upon release, leading to reactions that produce CO₂ and H₂O. However, not all the CO, H₂, and CH₄ partake in oxidation reactions due to the regulated oxygen supply. Devolatilization also produces char, which reacts with O₂, CO, CO₂, H₂O, and H₂ gas species. The effectiveness of the char reaction (heterogeneous reaction) with oxygen is not as pronounced as that of CO, H₂, and CH₄, given that homogeneous

reactions are significantly faster than heterogeneous ones. Nevertheless, char reactions with CO_2 and H_2O play a significant role in the production of CO and H_2 .

- Velocity profile

According to the velocity profile pattern, the particles with the highest speed (see Figure 9) were found in the central zone of the concentric area. This occurred because the middle concentric area had a higher particle velocity. On the contrary, particles enter the reactor's devolatilization (pyrolysis) zone at a slower speed due to the wider space compared to the combustion zone. The center of the pyrolysis zone displayed a slightly brighter blue color, indicating lower velocity in this area—the highest turbulence-influenced particle velocities within the reduction zone in the concentric center. Consequently, particles in the center moved faster than those along the wall. This suggests that particles introduced into the reactor from the center moved more quickly than those closer to the sides. The variation in particle velocity inside the reactor ranged from 0.16 to 3 m/s.

- Temperature profile

Figure 10 displays the temperature distributions for the vertical sections of the reactor. The temperature distribution in the vertical section was not uniform, primarily because of the uneven fluid field. Additionally, while the air inlet and gas outlet were geometrically symmetrical, the overall shape of the reactor was irregular.

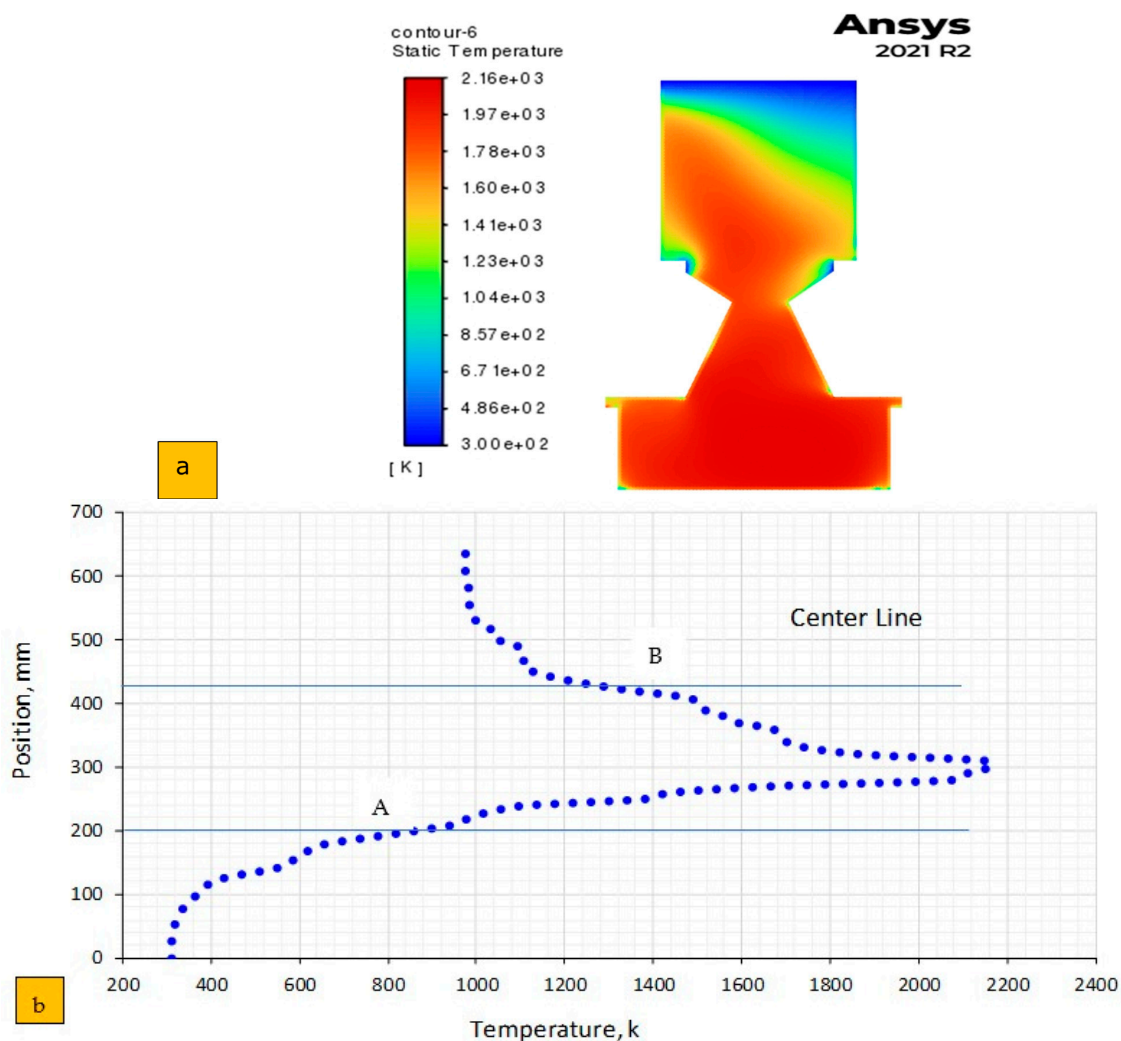


Figure 10. Temperature profile: (a) contour, and (b) center line.

The developed model utilized the non-premix combustion technique as the source term for reacting particles. This technique focused on the area of the diffusive flame, where the highest turbulence in the fuel–oxidizer mixture occurred. The mixture fraction was the hottest in this zone, and temperature increased with proximity to the flame. Consequently, a rich flame region emerged due to the highest concentration of the fuel–oxidizer mixture during combustion. A central line along the bed was selected to assess the temperature profile inside the reactor (see Figure 10).

In Figure 10, a specific temperature curve is depicted. The flame appeared dark yellow across the combustion and reduction zones. Even though particles existed in the combustion zone, their temperature varied, indicating rich (concentrated) flames. The flame temperature was approximately 2100 K (1827 °C) in both the reduction and combustion zones. The cooler region corresponded to the pyrolysis area, with a temperature range of 400 to 750 K (117 to 470 °C) at the beginning of devolatilization [63]. The results of this study were consistent with Gerun, Paraschiv [71], who developed a 2D axisymmetric CFDs model for the oxidation zone in a downdraft reactor.

In Figure 10b, the centerline temperature inside the reactor is presented, where point A marks the end of the pyrolysis zone, and B is the end point of the combustion zone. Table 9 indicates that the maximum temperature occurred in the combustion zone due to the exothermic reaction initiation [72]. In contrast, lower temperatures were observed in drying and pyrolysis, ranging from 300 to 856 K due to an endothermic reaction. A similar endothermic response also occurred in the bottom zone (reduction zone) [73]. Janajreh and Al Shrah [63] studied a different model (the Species Transport Reaction model) for the same reactor design and found a reduction temperature of 1273 K, consistent with the present study's results.

Table 9. CFDs simulation temperature at air–fuel ratio 6:1 and ER = 0.35.

Zone	Temperature Range, K
Drying and pyrolysis	300~856
Combustion	856~1356 (max temp. 2160)
Reduction	1356~974

- Model limitation for temperature

This model had limitations in predicting temperatures in specific areas, such as the middle section of the ash residue beneath the grate and the pressure outlet zone (see Figure 10). While the flame and predicted temperature in the char ash residual area suggested the possibility of further reactions, this could not be accurately forecasted. This uncertainty could significantly increase the temperature in the gas crawling area (narrow space) beneath the pressure exit. The char and ash are typically removed from the reactor automatically, but the model did not simulate this feature. Therefore, the temperature limitation and lack of char removal are critical for a combustion model.

Another drawback of the current model was that it inaccurately projected continuous burning (uneven), causing high turbulence in the gas crawling space. In real situations, this does not happen; instead, a vacuum pump draws the gas products with a moderate temperature of less than 600 K, contrasting with the model's prediction of over 1273 K.

- Gas density profile

The model incorporates a Probability Density Function (PDF) to account for the fluctuations in the mixing fraction. This parameter represents the ratio of unburned fuel to the entire mixture at any given point. In turbulent regions, where high temperatures prevail, the PDF predicts a lower probability of encountering unburned fuel than in calmer areas. This reflects the efficient mixing in turbulent zones, leading to a more complete combustion process.

According to this concept, the flame is characterized by the lowest density and the most turbulence, while denser particles tend to move closer to the wall. Figure 11 illustrates

the density contour (a) and centerline mass fraction (b) of the pellet during the combustion simulation. Here, it is noted that the gas fraction, known as the gas mass fraction, refers to the proportion of a specific gas relative to the total gas mixture within a chamber. The density of a gas directly correlates with its gas fraction. In other words, a higher gas fraction results in a higher density; conversely, a lower gas fraction leads to a lower density. In the pyrolysis zone, the mass fraction of solid particles appeared dark yellow, indicating a possibly unburned feedstock with moisture content and ash mixture compared to the reduction and char regions (yellow color).

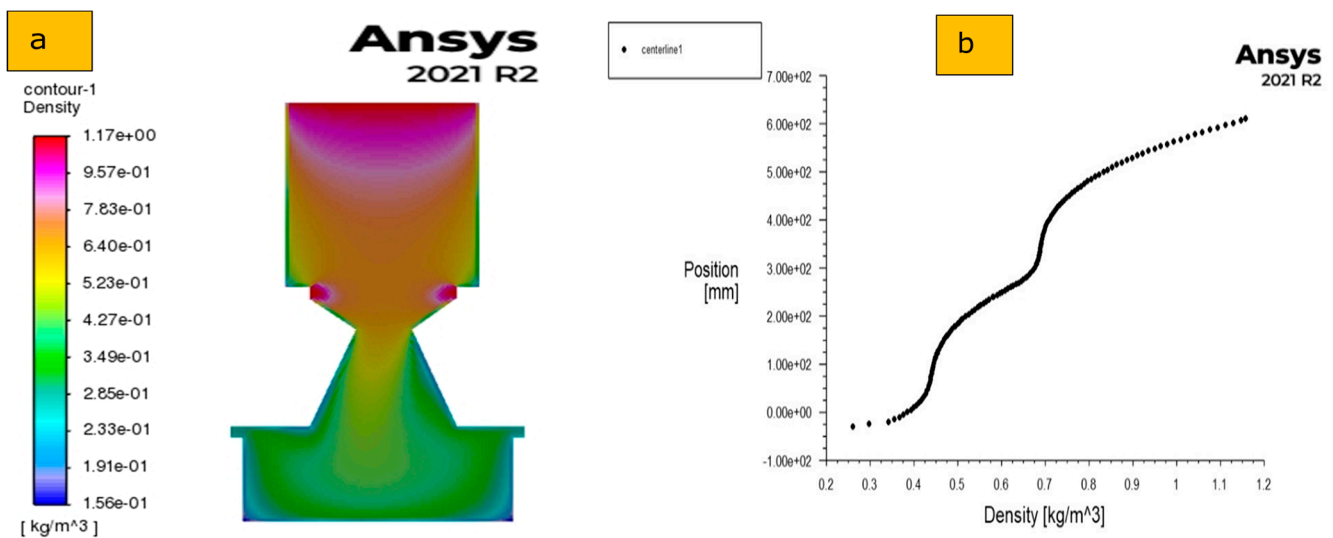


Figure 11. Density profile: (a) contour, and (b) centerline.

However, the outer wall had the maximum portion of unburned carbon. The mass fraction of unburnt carbon gradually decreased towards the concentric space. Inside the reactor, the particle density varied from 0.156 to 1.17 kg/m³ (Figure 11). This outcome aligns with a study on biomass pellet combustion by Boman, Nordin [74], which used a parametric dispersion model.

Janajreh and Al Shrah [63] have developed a computer model for a downdraft reactor, which is a larger version. They used a method that considers the movement of different chemical substances. According to their findings, solid char significantly decreased immediately after the combustion zone and continued declining to the reactor's bottom. They also observed a similar pattern for the profiles of unburned carbon, even though they used a different method to model the chemical reactions compared to the approach used in the current study.

- Pressure profile

The pressure profile contour in Figure 12 displays how pressure is distributed inside a downdraft reactor under specific operating conditions. Although the reactor operates at normal atmospheric pressure, the pressure within its inner shell changes as it produces a gaseous combustion product. The static pressure (pressure without motion) ranged from 0.766 to 3.53 Pascal as you move up the height of the reactor.

Figure 12b shows explicitly how the pressure varies along the centerline at different heights within the reactor due to the gravitational force and the downward movement of the feedstock along with the produced gas. The pressure is low at the biomass input point (660 mm from the bottom). As the biomass descends into the reactor, the pressure increases and reaches 2.75 Pascal at the bottom. Finally, the generated gas exits through the outlet at a reduced pressure. This means that pressure changes at different heights in the reactor due to the gravitational force and the downward movement of the feedstock along with

the produced gas, aligning with findings from Gupta, Jain [50], who simulated a 10 kW electric biomass downdraft reactor for woody biomass using a 2D model.

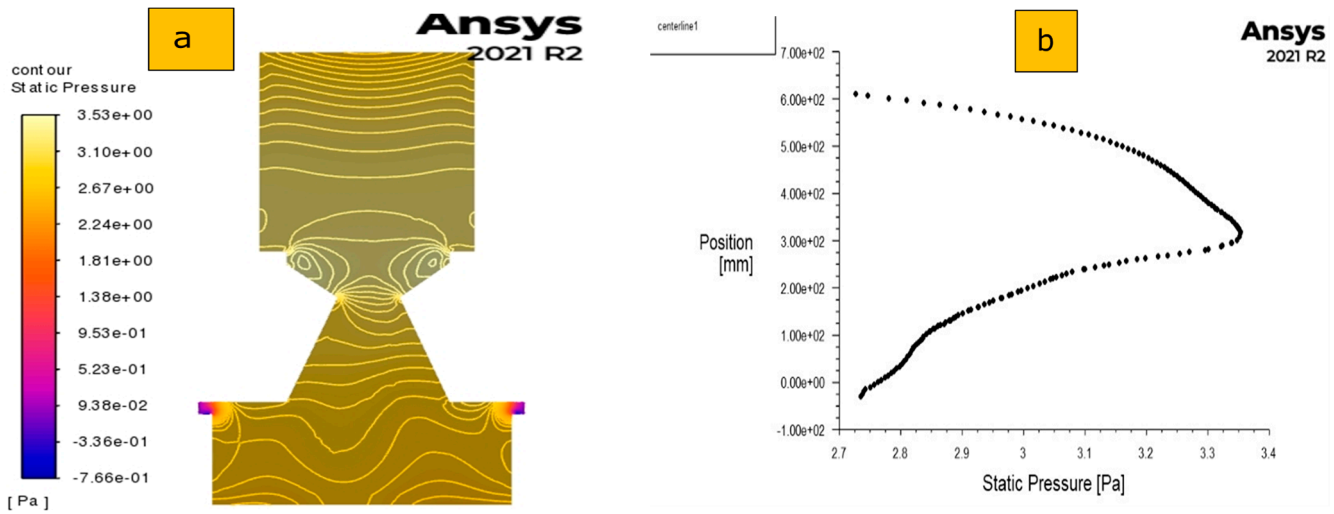


Figure 12. Static pressure profile: (a) contour, and (b) centerline.

- Gas species profile

Three main parts are formed during the complex process of turning biomass into gas: light gases, ashes (chars), and condensates. In a specific type of reactor called a downdraft reactor, where the amount of air supplied is fixed to a particular ratio (ER 0.35), Figures 13 and 14 illustrate how these gas fractions are distributed. The most important fraction among these is the light gases, making up more than 70% by weight. These light gases include carbon monoxide (CO), hydrogen (H₂), methane (CH₄), carbon dioxide (CO₂), and nitrogen (N₂), as mentioned in a study by Monteiro, Ismail [75].

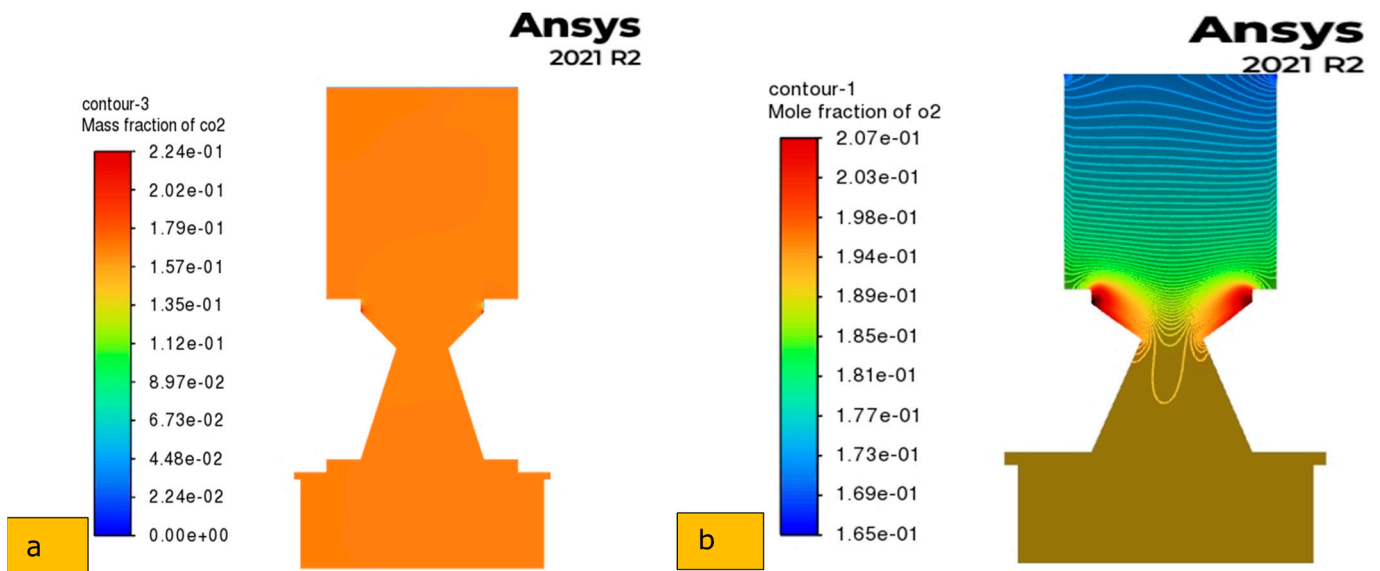


Figure 13. Gas species contour: (a) CO₂ and (b) O₂ mole fraction.

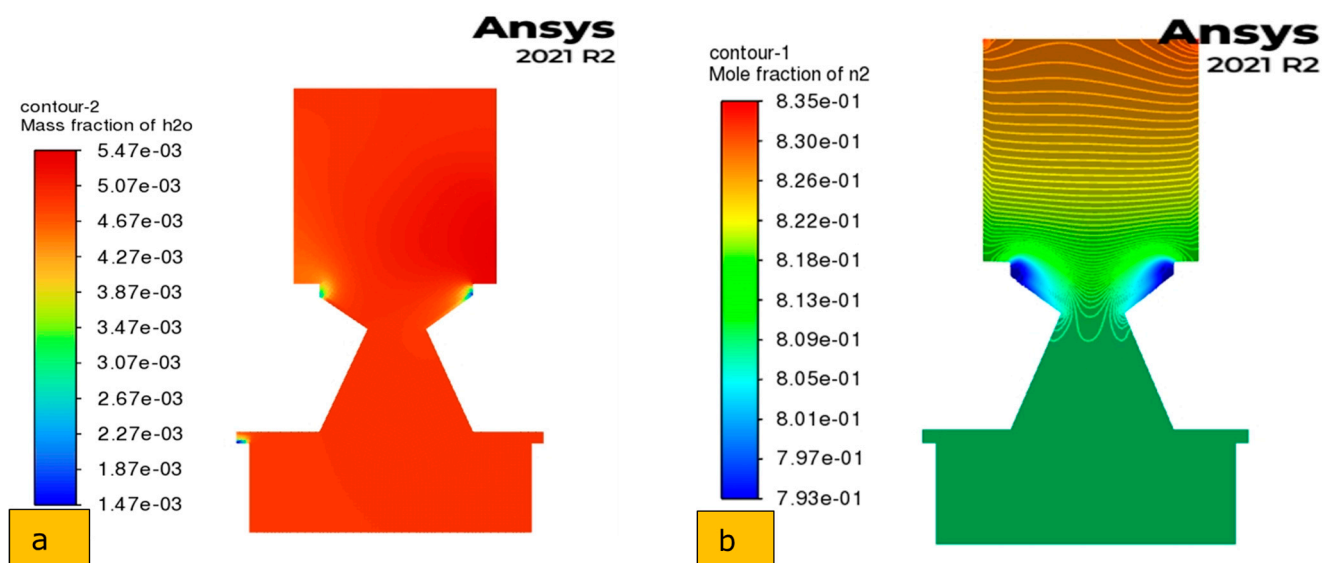


Figure 14. Gas species contour: (a) H₂O and (b) N₂ mole fraction.

- CO₂ and O₂ profile

Figure 13 displays the contours (patterns) of CO₂ and O₂. It indicates a slightly higher amount of CO₂ in the pyrolysis region, peaking in the flame zone. On the other hand, O₂ is more concentrated near the flash combustion zone and increases at the bottom of the reduction zone. The concentration of O₂ is highest near the air inlet (shown in red), while CO₂ is lowest there. Additionally, the burning of certain substances produces CO₂.

In the reactor, higher regions use up O₂, producing the heat needed for specific chemical processes. This observation might apply specifically to a type of combustion process called downdraft combustion, which uses air as the oxidizing agent. The contours of CO₂ and O₂ exhibit similar behaviors, although their concentrations may vary in observation. These findings align with a previous study by Zhou, Wang [76].

- H₂O and N₂ mole fraction profile

Figure 14 illustrates the contours for H₂O and N₂. In both profiles, the concentration was higher at the bottom of the reactor. The mole fraction of H₂O inside the reactor was almost consistent. However, the movement of N₂ was notably higher (about 0.82%) in the pyrolysis zone. Air entered the air inlet, where the N₂ concentration was also higher (Figure 14). Comparatively, Janajreh and Al Shrah [63] reported N₂ concentrations of 25.76% for non-adiabatic and 37.29% for adiabatic equilibrium reactions. The current study's results were higher, possibly due to using different feedstock (WSPs).

3.4. Performance Study

Operating conditions directly affect the reactor's performance. The following study investigated how temperature and the Equivalence Ratio (ER) impact gas production.

3.4.1. Effect of ER on Gas Composition

The Equivalence Ratio (ER) plays an important role in shaping the behavior of oxidation and reduction reactions in combustion processes. In reduction reactions, a smaller amount of char is involved. In contrast, oxidation reactions involve a more significant amount of char, leading to decreased CO and H₂ production, which might be associated with the chemical kinetic. The ER also influences the distribution of mole fractions within the reactor. Higher ER values result in increased delivery of O₂ and N₂ inside the reactor, elevating the nitrogen concentration and reducing the mole fraction of producer gas [65]. The mole fraction of gases determines the gas quality in the producer gas, and the ER significantly impacts this.

Figure 15 illustrates the mole fraction of producer gas at various ER values, ranging from 0.25 to 0.60, with a step value of 0.05. Lower ER values may occasionally result in incomplete combustion or produce producer gas with a low heating value and substantial char formation. Conversely, complete combustion occurs at ER = 1; in our study, ER = 0.6 indicates an operation condition near the combustion regime. On the other hand, the LHV gas is higher for lower ER values. The observations in Figure 15 support the notion that CO, H₂, and CH₄ levels decrease as ER increases due to the favoring of oxidation reactions [77]. A slight decrease in hydrocarbons (CH₄) was also observed for a similar reason.

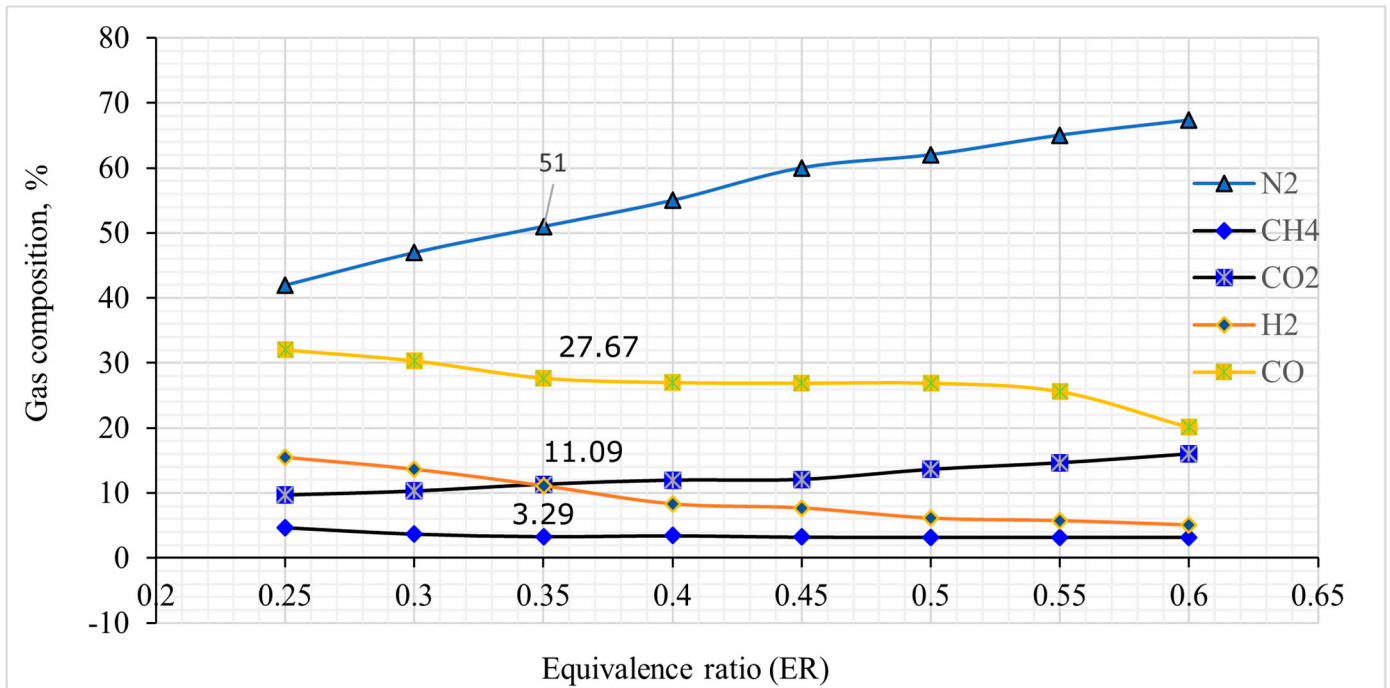


Figure 15. Gas composition at different equivalence ratios.

In contrast, CO₂ and N₂ levels increased with higher ER values, aligning with findings in the existing literature [78,79]. Consequently, an ER of 0.35 appeared to be optimal for gas production.

3.4.2. Estimation of Gas Generation and Gas Efficiency

Table 10 offers predictions for the average gas species fraction generated. Consider a gas yield (F_{gas}) of approximately 1.6 to 2.5 m³/kg of fuel pellets when calculating gas conversion efficiencies. This reference value was derived from experimental data on the combustion of different biomass pellets in a downdraft reactor with air-to-fuel ratios ranging from 1.1 to 1.4, as reported by Erlich and Fransson [65]. Additionally, note that the heating value of WSP is 19.06 MJ/kg (Table 1).

Table 10. Species gas composition for ER = 0.35.

Items	Value							
ER, %	0.25	0.30	0.35	0.40	0.45	0.50	0.55	0.60
LHV, MJ/kg	7.65	6.86	6.09	5.74	5.57	5.39	5.18	4.38
$E_{ff_{gas}}$, %	64~100	58~90	51~80	48~75	47~73	45~71	43~68	37~57

Note: ER = equivalence ratio; LHV = lower heating value of gas. $E_{ff_{gas}}$ = production gas conversion efficiency.

Table 10 also illustrates the Lower Heating Values (LHVs) obtained from CFDs simulations at different Equivalence Ratios (ER). The LHVs ranged from 4.38 to 7.65. These

findings align with prior research [80] even though they employed a 3D CFDs model with solid fuel (Miscanthus briquettes). The gas conversion efficiencies during WSP combustion varied from 51 to 80%, closely resembling the experimental hardwood pellet combustion results of Brar, Singh [79]. The authors used the same reactor (GEK 10 kW) for hardwood pellet combustion, recording a temperature of approximately 1473 K (1200 °C). Their findings indicated that 21% of the mixture was CO, while 11%, 16%, and 2% were CO₂, H₂, and CH₄, respectively. Overall, this model provides a reasonably accurate prediction of WSP combustion efficacy in the GEK 10 kW reactor.

3.4.3. Effect of Temperature on Gases Species Concentration

This CFDs model incorporated theoretical aspects like the devolatilization rate, volatile decomposition scheme, oxidation, and reduction reactions, drawing from previous studies [81]. The model also considered the gas phase and solid particle reactions driven by temperature variations in the reactor (Table 3) [82].

This study predicts the gas composition in a downdraft reactor with an Equivalence Ratio (ER) of 0.35. Utilizing the CFDs model, the gas composition across a temperature range of 770 to 1480 K for WSPs on a dry basis was calculated. Notably, the N₂ content increased slightly, while the CO concentration increased at higher temperatures (Figure 16). Simultaneously, concentrations of H₂ and CO₂ decreased with rising temperatures. Furthermore, a CH₄ concentration of zero beyond 1173 K suggests that the chemical reaction likely concluded due to the high temperature (1173 K) of combustion. CH₄ concentration dropped to 0 beyond 1173 K during the biochar/char decomposition; it was observed that there was almost no presence of CH₄, indicating the possibility of no chemical reaction occurring. These findings align with observations in the literature, as reported by Antonopoulos, Karagiannidis [83], and Mathieu and Dubuisson [84].

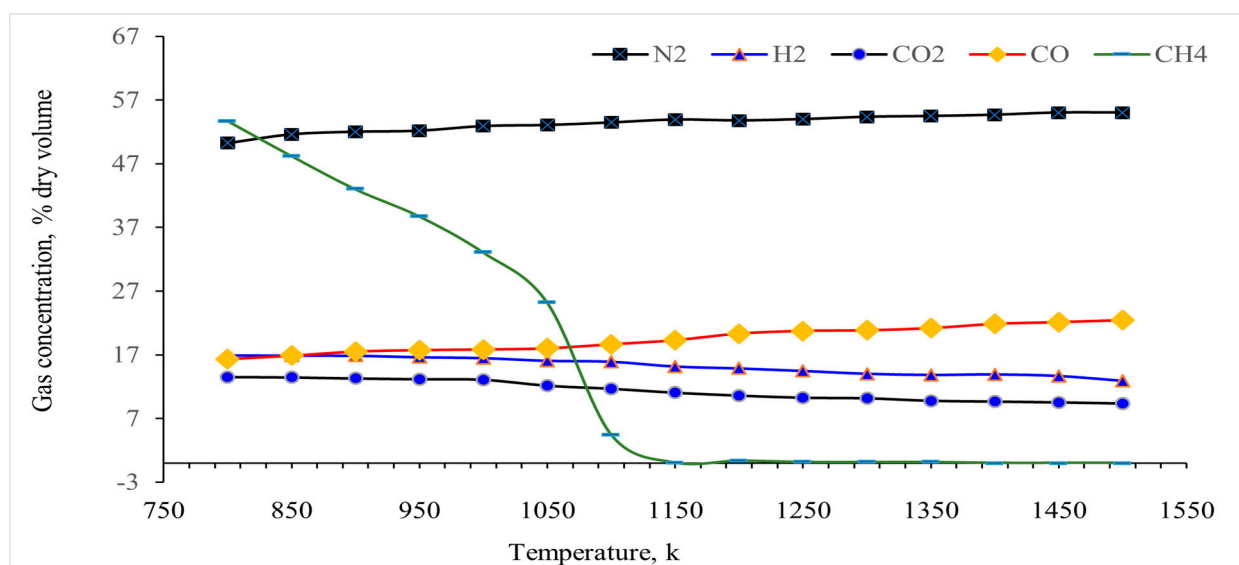


Figure 16. Effect of temperature on gas species.

4. Conclusions

This study utilized a 2D CFDs model to simulate the combustion process of wheat straw pellets (WSPs) in a fixed-bed downdraft reactor. The simulation incorporated a discrete phase particle model, a non-premix combustion process, and a $k-\epsilon$ turbulence model.

The ANSYS Fluent 2021R2 tool was used to investigate the impact of the Equivalence Ratio (ER) and temperature on gas composition. The model results were initially compared and validated against experimental data. The mathematical model agreed well with the experimental results concerning temperature and producer gas (CO₂, CO, CH₄). However,

in the case of H₂ gas, there are differences between simulation and experiment results, necessitating a reassessment of model assumptions.

This study explored predicting variations in temperature, pressure, and velocity within the reactor. Based on the numerical predictions, several conclusions were drawn:

- A higher temperature zone prevails beneath the air injection area.
- Changes in the Equivalence Ratio influenced the heating value of gas and gas production efficiency.
- An ER of 0.35 appeared optimal for maximizing gas production efficiency.
- An increased ER led to a decrease in CO and H₂ composition and increased CO₂ concentration.
- A higher equivalence ratio (0.25~0.6) is responsible for the high nitrogen content (42~67.3%) in producer gas.

These results provide valuable insights for improving the performance of fixed-bed reactors using wheat straw pellets as a sustainable fuel source. This study offers important information on optimizing combustion parameters to achieve efficient and clean gas production. However, further research could be needed as follows:

- Validating the CFDs model for different reactor geometries or operating conditions.
- Investigating the influence of additional factors like particle size or moisture content on combustion behavior.
- Optimizing reactor design for improved heat transfer and gas production yield.

Author Contributions: Conceptualization, B.N. and G.C.; software, B.N.; methodology, B.N.; investigation, B.N.; writing—original draft, B.N.; supervision, G.C. and L.B.; writing—review and editing, G.C. and L.B.; data curation, R.A.M. All authors have read and agreed to the published version of the manuscript.

Funding: The National Agricultural Technology Program Phase-II, Bangladesh Agricultural Research Council (BARC), Farmgate, Dhaka 1215, Bangladesh, financially supported this work.

Data Availability Statement: Data are contained within the article.

Acknowledgments: The authors thank the University of Southern Queensland (UniSQ), QLD, Australia, for its research facility.

Conflicts of Interest: The authors declare that they have no known competing financial interests or personal relationships that could have appeared to influence the work reported in this paper.

Nomenclature

ρ = the density of the fluid mixture	t = time
Y_k = mass fraction of species k in the fluid mixtures	p = pressure
Y_m = fluctuation dilation in compressible turbulence	$\mu_i\mu_j$ = velocity components
f_{kj} = volume force acting on species k in the j direction	τ_{ij} = the viscus stress tensor
$x_i x_j$ = coordinates axes	∂_{ij} = the tensor unit
μ = dynamic viscosity of the mixture	ω_k = the reaction rate of species k
V_{ki} = the i -component of the diffusion velocity of species k	S_k = user-defined source terms for k
q_i = energy flux in the mixture	S_ϵ = user-defined source term for ϵ
e_t = total energy from chemical, potential, and kinetic energies	σ_k = turbulent Prandtl numbers for k
\dot{Q} = energy flux from the outer heating source	σ_ϵ = turbulent Prandtl numbers for ϵ
S_i = source term for the i -th (x, y, z) momentum equation	h = sensible enthalpy
C_p = specific heat at constant pressure	ΔH = latent heat enthalpy
R_i = net rate of production of species, i	h_{ref} = reference enthalpy
R_i = net rate of production of species " i " by chemical reaction	T_{ref} = reference temperature
C_p = specific heat	Y_i = species i 's average mass
G_b = turbulence kinetic energy due to buoyancy	f_v = volatile fraction

C = linear-anisotropic phase function coefficient

h_{fg} = latent heat of evaporation

σ = Stefan constant, respectively.

$F_D(\vec{\mu} - \vec{\mu}_p)$ = drag force per unit particle mass.

m_p^0 = initial mass

α = absorption coefficient

σ_s = Stefan–Boltzmann constant, 5.67×10^{-8} (W/(m²·K⁴))

G = incident radiation

A = particle surface area

References

1. Giwa, A.; Alabi, A.; Yusuf, A.; Olukan, T. A comprehensive review on biomass and solar energy for sustainable energy generation in Nigeria. *Renew. Sustain. Energy Rev.* **2016**, *69*, 620–641. [[CrossRef](#)]
2. Pandey, B.; Prajapati, Y.K.; Sheth, P.N. CFD analysis of biomass gasification using downdraft gasifier. *Mater. Today Proc.* **2020**, *44*, 4107–4111. [[CrossRef](#)]
3. Ahrenfeldt, J.; Thomsen, T.P.; Henriksen, U.; Clausen, L.R. Biomass gasification cogeneration—A review of state of the art technology and near future perspectives. *Appl. Therm. Eng.* **2013**, *50*, 1407–1417. [[CrossRef](#)]
4. Bahng, M.-K.; Mukarakate, C.; Robichaud, D.J.; Nimlos, M.R. Current technologies for analysis of biomass thermochemical processing: A review. *Anal. Chim. Acta* **2009**, *651*, 117–138. [[CrossRef](#)] [[PubMed](#)]
5. Caputo, A.C.; Palumbo, M.; Pelagagge, P.M.; Scacchia, F. Economics of biomass energy utilization in combustion and gasification plants: Effects of logistic variables. *Biomass-Bioenergy* **2005**, *28*, 35–51. [[CrossRef](#)]
6. Jahromi, R.; Rezaei, M.; Samadi, S.H.; Jahromi, H. Biomass gasification in a downdraft fixed-bed gasifier: Optimization of operating conditions. *Chem. Eng. Sci.* **2020**, *231*, 116249. [[CrossRef](#)]
7. Susastriawan, A.; Saptoadi, H. Purnomo Small-scale downdraft gasifiers for biomass gasification: A review. *Renew. Sustain. Energy Rev.* **2017**, *76*, 989–1003. [[CrossRef](#)]
8. Silva, J.; Teixeira, J.; Teixeira, S.; Preziati, S.; Cassiano, J. CFD Modeling of Combustion in Biomass Furnace. *Energy Procedia* **2017**, *120*, 665–672. [[CrossRef](#)]
9. Gómez, M.; Porteiro, J.; Patiño, D.; Míguez, J. CFD modelling of thermal conversion and packed bed compaction in biomass combustion. *Fuel* **2014**, *117*, 716–732. [[CrossRef](#)]
10. El-Sayed, S.A.; Khass, T.M.; Noseir, E.H.; Ismail, M.A.; Mostafa, M.E. Combustion Characteristics and Visualization Analysis of a Biomass Pellet Oriented in Different Positions in a Fixed-Bed Reactor at Different Operating Conditions. *Ind. Eng. Chem. Res.* **2023**, *62*, 4281–4296. [[CrossRef](#)]
11. Baruah, D. Modeling of biomass gasification: A review. *Renew. Sustain. Energy Rev.* **2014**, *39*, 806–815. [[CrossRef](#)]
12. Patra, T.K.; Sheth, P.N. Biomass gasification models for downdraft gasifier: A state-of-the-art review. *Renew. Sustain. Energy Rev.* **2015**, *50*, 583–593. [[CrossRef](#)]
13. Dhanavath, K.N.; Shah, K.; Bhargava, S.K.; Bankupalli, S.; Parthasarathy, R. Oxygen–steam gasification of karanja press seed cake: Fixed bed experiments, ASPEN Plus process model development and benchmarking with saw dust, rice husk and sunflower husk. *J. Environ. Chem. Eng.* **2018**, *6*, 3061–3069. [[CrossRef](#)]
14. La Villetta, M.; Costa, M.; Massarotti, N. Modelling approaches to biomass gasification: A review with emphasis on the stoichiometric method. *Renew. Sustain. Energy Rev.* **2017**, *74*, 71–88. [[CrossRef](#)]
15. Ahmed, T.Y.; Ahmad, M.M.; Yusup, S.; Inayat, A.; Khan, Z. Mathematical and computational approaches for design of biomass gasification for hydrogen production: A review. *Renew. Sustain. Energy Rev.* **2012**, *16*, 2304–2315. [[CrossRef](#)]
16. Liu, H.; Elkamel, A.; Lohi, A.; Biglari, M. Computational Fluid Dynamics Modeling of Biomass Gasification in Circulating Fluidized-Bed Reactor Using the Eulerian–Eulerian Approach. *Ind. Eng. Chem. Res.* **2013**, *52*, 18162–18174. [[CrossRef](#)]
17. Chogani, A.; Moosavi, A.; Sarvestani, A.B.; Shariat, M. The effect of chemical functional groups and salt concentration on performance of single-layer graphene membrane in water desalination process: A molecular dynamics simulation study. *J. Mol. Liq.* **2020**, *301*, 112478. [[CrossRef](#)]
18. Wang, Y.; Yan, L. CFD Studies on Biomass Thermochemical Conversion. *Int. J. Mol. Sci.* **2008**, *9*, 1108–1130. [[CrossRef](#)]
19. Wu, Y.; Zhang, Q.; Yang, W.; Blasiak, W. Two-Dimensional Computational Fluid Dynamics Simulation of Biomass Gasification in a Downdraft Fixed-Bed Gasifier with Highly Preheated Air and Steam. *Energy Fuels* **2013**, *27*, 3274–3282. [[CrossRef](#)]
20. Poletto, M.; Dettenborn, J.; Pistor, V.; Zeni, M.; Zattera, A.J. Materials produced from plant biomass: Part I: Evaluation of thermal stability and pyrolysis of wood. *Mater. Res.* **2010**, *13*, 375–379. [[CrossRef](#)]
21. Fernando, N.; Narayana, M. A comprehensive two dimensional Computational Fluid Dynamics model for an updraft biomass gasifier. *Renew. Energy* **2016**, *99*, 698–710. [[CrossRef](#)]
22. El-Shafay, A.; Hegazi, A.; Zeidan, E.; El-Emam, S.; Okasha, F. Experimental and numerical study of sawdust air-gasification. *Alex. Eng. J.* **2020**, *59*, 3665–3679. [[CrossRef](#)]
23. Gupta, S.; Gupta, G.K.; Mondal, M.K. Thermal degradation characteristics, kinetics, thermodynamic, and reaction mechanism analysis of pistachio shell pyrolysis for its bioenergy potential. *Biomass-Convert. Biorefinery* **2020**, *12*, 4847–4861. [[CrossRef](#)]
24. Chaney, J.; Liu, H.; Li, J. An overview of CFD modelling of small-scale fixed-bed biomass pellet boilers with preliminary results from a simplified approach. *Energy Convers. Manag.* **2012**, *63*, 149–156. [[CrossRef](#)]
25. Pandey, B.; Prajapati, Y.K.; Sheth, P.N. CFD analysis of the downdraft gasifier using species-transport and discrete phase model. *Fuel* **2022**, *328*, 125302. [[CrossRef](#)]

26. Meenaroch, P.; Kerdsuwan, S.; Laohalidanond, K. Development of Kinetics Models in Each Zone of a 10kg/hr Downdraft Gasifier using Computational Fluid Dynamics. *Energy Procedia* **2015**, *79*, 278–283. [CrossRef]
27. Ngamsidhiphongsas, N.; Ponpesh, P.; Shotipruk, A.; Arpornwichanop, A. Analysis of the Imbert downdraft gasifier using a species-transport CFD model including tar-cracking reactions. *Energy Convers. Manag.* **2020**, *213*, 112808. [CrossRef]
28. Wu, X.; Gong, Y.; Guo, Q.; Xue, Z.; Yu, G. Experimental study on the atomization and particle evolution characteristics in an impinging entrained-flow gasifier. *Chem. Eng. Sci.* **2019**, *207*, 542–555. [CrossRef]
29. Chapela, S.; Porteiro, J.; Míguez, J.L.; Behrendt, F. Eulerian CFD fouling model for fixed bed biomass combustion systems. *Fuel* **2020**, *278*, 118251. [CrossRef]
30. Ma, Y.; Khan, M.Z.; Liu, Y.; Xiao, J.; Chen, X.; Ji, S.; Cao, Z.; Li, S. Analysis of Nutrient Composition, Rumen Degradation Characteristics, and Feeding Value of Chinese Rye Grass, Barley Grass, and Naked Oat Straw. *Animals* **2021**, *11*, 2486. [CrossRef]
31. Álvarez-Bermúdez, C.; Chapela, S.; Varela, L.G.; Gómez, M.Á. CFD simulation of an internally cooled biomass fixed-bed combustion plant. *Resources* **2021**, *10*, 77. [CrossRef]
32. Zhang, J.; Li, T.; Ström, H.; Løvås, T. Computationally efficient coarse-graining XDEM/CFD modeling of fixed-bed combustion of biomass. *Combust. Flame* **2021**, *238*, 111876. [CrossRef]
33. Zainal, Z.; Rifau, A.; Quadir, G.; Seetharamu, K. Experimental investigation of a downdraft biomass gasifier. *Biomass-Bioenergy* **2002**, *23*, 283–289. [CrossRef]
34. Vidian, F.; Sampurno, R.D. Cfd Simulation of Sawdust Gasification on Open Top Thr Oatless Downdraft Gasifier. *J. Mech. Eng. Res. Dev.* **2018**, *41*, 106–110.
35. Hsi, C.-L.; Kuo, J.-T. Estimation of fuel burning rate and heating value with highly variable properties for optimum combustion control. *Biomass-Bioenergy* **2008**, *32*, 1255–1262. [CrossRef]
36. Mätzing, H.; Gehrman, H.-J.; Seifert, H.; Stapf, D. Modelling grate combustion of biomass and low rank fuels with CFD application. *Waste Manag.* **2018**, *78*, 686–697. [CrossRef] [PubMed]
37. Bhuiyan, A.A.; Karim, M.R.; Naser, J. Modeling of Solid and Bio-Fuel Combustion Technologies. In *Thermofluid Modeling for Energy Efficiency Applications*; Elsevier: New York, NY, USA, 2016; pp. 259–309.
38. Nath, B.; Chen, G.; Bowtell, L.; Graham, E. An investigation of thermal decomposition behavior and combustion parameter of pellets from wheat straw and additive blends by thermogravimetric analysis. *Int. J. Thermofluids* **2024**, *22*, 100660. [CrossRef]
39. Nath, B.; Chen, G.; Bowtell, L.; Graham, E. Kinetic mechanism of wheat straw pellets combustion process with a thermogravimetric analyser. *Heliyon* **2023**, *9*, e20602. [CrossRef]
40. Nath, B.; Chen, G.; Bowtell, L.; Mahmood, R.A. Assessment of densified fuel quality parameters: A case study for wheat straw pellet. *J. Bioresour. Bioprod.* **2023**, *8*, 45–58. [CrossRef]
41. Mahinpey, N.; Gomez, A. Review of gasification fundamentals and new findings: Reactors, feedstock, and kinetic studies. *Chem. Eng. Sci.* **2016**, *148*, 14–31. [CrossRef]
42. Siripaiboon, C.; Sarabhorn, P.; Areeprasert, C. Two-dimensional CFD simulation and pilot-scale experimental verification of a downdraft gasifier: Effect of reactor aspect ratios on temperature and syngas composition during gasification. *Int. J. Coal Sci. Technol.* **2020**, *7*, 536–550. [CrossRef]
43. Dupont, C.; Boissonnet, G.; Seiler, J.-M.; Gauthier, P.; Schweich, D. Study about the kinetic processes of biomass steam gasification. *Fuel* **2007**, *86*, 32–40. [CrossRef]
44. Pérez, J.F.; Melgar, A.; Benjumea, P.N. Effect of operating and design parameters on the gasification/combustion process of waste biomass in fixed bed downdraft reactors: An experimental study. *Fuel* **2012**, *96*, 487–496. [CrossRef]
45. Nørregaard, A.; Bach, C.; Krühne, U.; Borgbjerg, U.; Gernaey, K.V. Hypothesis-driven compartment model for stirred bioreactors utilizing computational fluid dynamics and multiple pH sensors. *Chem. Eng. J.* **2018**, *356*, 161–169. [CrossRef]
46. Abele, E.; Fujara, M. Simulation-based twist drill design and geometry optimization. *CIRP Ann.* **2010**, *59*, 145–150. [CrossRef]
47. ANSYS. *ANSYS Fluent Theory Guide*; ANSYS, Inc.: Canonsburg, PA, USA, 2015.
48. Yang, Q.; Cheng, K.; Wang, Y.; Ahmad, M. Improvement of semi-resolved CFD-DEM model for seepage-induced fine-particle migration: Eliminate limitation on mesh refinement. *Comput. Geotech.* **2019**, *110*, 1–18. [CrossRef]
49. Kumar, A.; Jones, D.D.; Hanna, M.A. Thermochemical Biomass Gasification: A Review of the Current Status of the Technology. *Energies* **2009**, *2*, 556–581. [CrossRef]
50. Gupta, R.; Jain, P.; Vyas, S. CFD modeling and simulation of 10 kWe Biomass Downdraft gasifier. *Int. J. Curr. Eng. Technol.* **2017**, *7*, 1446–1452.
51. Barone, G.; Martelli, D. Validation of the Coupled Calculation between RELAP5 STH Code and Ansys FLUENT CFD Code. 2014. Available online: <https://iris.enea.it/retrieve/handle/20.500.12079/7726/1350/ADPFISS-LP2-076.pdf> (accessed on 23 January 2024).
52. Wu, C.-C.; Völker, D.; Weisbrich, S.; Neitzel, F. The finite volume method in the context of the finite element method. *Mater. Today Proc.* **2022**, *62*, 2679–2683. [CrossRef]
53. ANSYS. *ANSYS Fluent Theory Guide*; ANSYS, Inc.: Canonsburg, PA, USA, 2018.
54. Lu, D.; Yoshikawa, K.; Ismail, T.M.; El-Salam, M.A. Assessment of the carbonized woody briquette gasification in an updraft fixed bed gasifier using the Euler-Euler model. *Appl. Energy* **2018**, *220*, 70–86. [CrossRef]
55. Launder, B.; Spalding, D. *Lectures in Mathematical Models of Turbulence*; Academic Press: London, UK, 1972.

56. Keshtkar, M.; Eslami, M.; Jafarpur, K. A novel procedure for transient CFD modeling of basin solar stills: Coupling of species and energy equations. *Desalination* **2020**, *481*, 114350. [[CrossRef](#)]
57. Magnussen, B.F.; Hjertager, B.H. *On Mathematical Modeling of Turbulent Combustion with Special Emphasis on Soot Formation and Combustion*; Elsevier: New, York, NY, USA, 1977.
58. Zhang, J.; Li, T.; Ström, H.; Løvås, T. Grid-independent Eulerian-Lagrangian approaches for simulations of solid fuel particle combustion. *Chem. Eng. J.* **2020**, *387*, 123964. [[CrossRef](#)]
59. Zhu, M.; Chen, X.; Zhou, C.-S.; Xu, J.-S.; Musa, O. Numerical Study of Micron-Scale Aluminum Particle Combustion in an Afterburner Using Two-Way Coupling CFD–DEM Approach. *Flow Turbul. Combust.* **2020**, *105*, 191–212. [[CrossRef](#)]
60. Lian, G.; Zhong, W. CFD–DEM modeling of oxy-char combustion in a fluidized bed. *Powder Technol.* **2022**, *407*, 117698. [[CrossRef](#)]
61. Luan, Y.-T.; Chyou, Y.-P.; Wang, T. Numerical analysis of gasification performance via finite-rate model in a cross-type two-stage gasifier. *Int. J. Heat Mass Transf.* **2013**, *57*, 558–566. [[CrossRef](#)]
62. Di Blasi, C. Dynamic behaviour of stratified downdraft gasifiers. *Chem. Eng. Sci.* **2000**, *55*, 2931–2944. [[CrossRef](#)]
63. Janajreh, I.; Al Shrah, M. Numerical and experimental investigation of downdraft gasification of wood chips. *Energy Convers. Manag.* **2013**, *65*, 783–792. [[CrossRef](#)]
64. Muilenburg, M.; Shi, Y.; Ratner, A. Computational Modeling of the Combustion and Gasification Zones in a Downdraft Gasifier. ASME 2011 International Mechanical Engineering Congress and Exposition. In Proceedings of the ASME International Mechanical Engineering Congress and Exposition, Denver, CO, USA, 11–17 November 2011; Volume 54907, pp. 151–158.
65. Erlich, C.; Fransson, T.H. Downdraft gasification of pellets made of wood, palm-oil residues respective bagasse: Experimental study. *Appl. Energy* **2011**, *88*, 899–908. [[CrossRef](#)]
66. Hwang, I.S.; Sohn, J.; Lee, U.D.; Hwang, J. CFD-DEM simulation of air-blown gasification of biomass in a bubbling fluidized bed gasifier: Effects of equivalence ratio and fluidization number. *Energy* **2020**, *219*, 119533. [[CrossRef](#)]
67. Barco-Burgos, J.; Carles-Bruno, J.; Eicker, U.; Saldana-Robles, A.; Alcántar-Camarena, V. Hydrogen-rich syngas production from palm kernel shells (PKS) biomass on a downdraft allothermal gasifier using steam as a gasifying agent. *Energy Convers. Manag.* **2021**, *245*, 114592. [[CrossRef](#)]
68. ANSYS. *ANSYS Fluent Theory Guide*; ANSYS Inc.: Canonsburg, PA, USA, 2019.
69. Maya, D.M.Y.; Lora, E.E.S.; Andrade, R.V.; Ratner, A.; Angel, J.D.M. Biomass gasification using mixtures of air, saturated steam, and oxygen in a two-stage downdraft gasifier. Assessment using a CFD modeling approach. *Renew. Energy* **2021**, *177*, 1014–1030. [[CrossRef](#)]
70. Murugan, P.C.; Sekhar, S.J. Species—Transport CFD model for the gasification of rice husk (*Oryza sativa*) using downdraft gasifier. *Comput. Electron. Agric.* **2017**, *139*, 33–40. [[CrossRef](#)]
71. Gerun, L.; Paraschiv, M.; Vijeju, R.; Bellettre, J.; Tazerout, M.; Gøbel, B.; Henriksen, U. Numerical investigation of the partial oxidation in a two-stage downdraft gasifier. *Fuel* **2008**, *87*, 1383–1393. [[CrossRef](#)]
72. Fang, Y.; Paul, M.C.; Varjani, S.; Li, X.; Park, Y.-K.; You, S. Concentrated solar thermochemical gasification of biomass: Principles, applications, and development. *Renew. Sustain. Energy Rev.* **2021**, *150*, 111484. [[CrossRef](#)]
73. Li, Z.; Xu, H.; Yang, W.; Zhou, A.; Xu, M. CFD simulation of a fluidized bed reactor for biomass chemical looping gasification with continuous feedstock. *Energy Convers. Manag.* **2019**, *201*, 112143. [[CrossRef](#)]
74. Boman, C.; Nordin, A.; Thaning, L. Effects of increased biomass pellet combustion on ambient air quality in residential areas—A parametric dispersion modeling study. *Biomass-Bioenergy* **2003**, *24*, 465–474. [[CrossRef](#)]
75. Monteiro, E.; Ismail, T.M.; Ramos, A.; El-Salam, M.A.; Brito, P.; Rouboa, A. Assessment of the miscanthus gasification in a semi-industrial gasifier using a CFD model. *Appl. Therm. Eng.* **2017**, *123*, 448–457. [[CrossRef](#)]
76. Zhou, L.; Wang, Y.; Huang, Q.; Cai, J. Thermogravimetric characteristics and kinetic of plastic and biomass blends co-pyrolysis. *Fuel Process. Technol.* **2006**, *87*, 963–969. [[CrossRef](#)]
77. Sheth, P.N.; Babu, B. Experimental studies on producer gas generation from wood waste in a downdraft biomass gasifier. *Bioresour. Technol.* **2009**, *100*, 3127–3133. [[CrossRef](#)]
78. Gungor, A.; Yildirim, U. Two dimensional numerical computation of a circulating fluidized bed biomass gasifier. *Comput. Chem. Eng.* **2013**, *48*, 234–250. [[CrossRef](#)]
79. Brar, J.S.; Singh, K.; Zondlo, J.; Wang, J. Co-gasification of Coal and Hardwood Pellets: Syngas Composition, Carbon Efficiency and Energy Efficiency. In *2012 Dallas, Texas, 29 July–1 August 2012*; American Society of Agricultural and Biological Engineers: St. Joseph, MI, USA, 2012.
80. Sharma, T.; Maya, D.M.Y.; Nascimento, F.R.M.; Shi, Y.; Ratner, A.; Lora, E.E.S.; Neto, L.J.M.; Palacios, J.C.E.; Andrade, R.V. An Experimental and Theoretical Study of the Gasification of Miscanthus Briquettes in a Double-Stage Downdraft Gasifier: Syngas, Tar, and Biochar Characterization. *Energies* **2018**, *11*, 3225. [[CrossRef](#)]
81. Kumar, U.; Paul, M.C. CFD modelling of biomass gasification with a volatile break-up approach. *Chem. Eng. Sci.* **2018**, *195*, 413–422. [[CrossRef](#)]
82. Di Blasi, C.; Branca, C. Modeling a stratified downdraft wood gasifier with primary and secondary air entry. *Fuel* **2013**, *104*, 847–860. [[CrossRef](#)]

-
83. Antonopoulos, I.-S.; Karagiannidis, A.; Gkouletsos, A.; Perkoulidis, G. Modelling of a downdraft gasifier fed by agricultural residues. *Waste Manag.* **2012**, *32*, 710–718. [[CrossRef](#)]
 84. Mathieu, P.; Dubuisson, R. Performance analysis of a biomass gasifier. *Energy Convers. Manag.* **2002**, *43*, 1291–1299. [[CrossRef](#)]

Disclaimer/Publisher’s Note: The statements, opinions and data contained in all publications are solely those of the individual author(s) and contributor(s) and not of MDPI and/or the editor(s). MDPI and/or the editor(s) disclaim responsibility for any injury to people or property resulting from any ideas, methods, instructions or products referred to in the content.